INTERNATIONAL JOURNAL FOR NUMERICAL METHODS IN FLUIDS
Int. J. Numer. Meth. Fluids 2002; **39**:549–583 (DOI: 10.1002/fld.234)

High-order upwinding and the hydraulic jump

V. G. Ferreira[1], M. F. Tomé[2], N. Mangiavacchi[2], A. Castelo[2], J. A. Cuminato[2], A. O. Fortuna[2] and S. McKee[3,*]

[1] *Departamento de Estatística, Matemática Aplicada e Computacional, IGCE—Instituto de Geociências e Ciências Exatas, UNESP, Rio Claro, SP, Brazil*
[2] *Departamento de Ciências de Computação e Estatística, ICMC—Instituto de Ciências Matemáticas e de Computação, USP, São Carlos, SP, Brazil*
[3] *Department of Mathematics, University of Strathclyde, Glasgow, U.K.*

SUMMARY

This work is concerned with the computation of incompressible axisymmetric and full three-dimensional free-surface flows. In particular, the circular-hydraulic jump is simulated and compared with approximate analytic solutions. However, the principal thrust of this paper is to provide a real problem as a test bed for comparing the many existing convective approximations. Their performance is compared; SMART, HLPA and VONOS emerge as acceptable upwinding methods for this problem. Copyright © 2002 John Wiley & Sons, Ltd.

KEY WORDS: Navier–Stokes; free-surface flows; finite differences; upwinding; high-order discretization; bounded numerical scheme; hydraulic jump

1. INTRODUCTION

Every housewife has seen a hydraulic jump: turning a tap causes a jet of water to flow vertically downwards, impinge onto a horizontal surface, the sink, and spread out laterally with an annular ridge appearing some distance from the point of impingement.

This paper is concerned with the simulation of the annular-hydraulic jump and with the use of this real and commercially important problem to effect a comparison between existing high-order upwind schemes. The simulations have been carried out using the axisymmetric GENSMAC code [1] and the fully 3D version, Freeflow3D [2, 3]; both codes were developed from GENSMAC [4], which in turn was strongly influenced by the Marker and Cell (MAC) [5] and the Simplified Marker and Cell (SMAC) [6], originating from Los Alamos in the 1960s.

* Correspondence to: S. McKee, Department of Mathematics, University of Strathclyde, Livingstone Tower, 26 Richmond Street, Glasgow G1 IXH, U.K.

Contract grant sponsor: FAPESP,CNPq and Royal Society of Edinburgh

Received July 2000
Revised June 2001

This paper begins with a discussion of our current understanding (and lack of understanding) of the hydraulic jump. Different approximations of the convective terms in the Navier–Stokes equations are discussed. Then the axisymmetric GENSMAC is introduced, simulations are performed and a comparison of the different upwinding techniques with Watson's [7] (approximate) analytic results is effected, suggesting reasonable qualitative agreement for the range of parameters for which the approximations are valid. This permitted a tentative ranking of the upwind approximants. The convection schemes are then extended to three dimensions, and the full 3D code, Freeflow3D, is applied for both planar and axisymmetric flows. It is shown to be capable of resolving the so-called Type I and Type II flows at the jump. Again, a comparison of various upwinding schemes is provided with evidence that SMART, HLPA and VONOS are the only three capable of simulating the jet flow for Reynolds numbers of the order of 1000.

2. THE HYDRAULIC JUMP

The hydraulic jump, or standing wave, is the stationary counterpart of the tidal bore (see Figure 1).

An understanding of the phenomenon is of commercial interest, since jet impingement is often used in cooling systems and the slow flow of the fluid beyond the jump can degrade the efficiency of the system. Despite this, the problem is not yet fully understood and does not appear to have been properly simulated (although see Yokoi and Xiao [8] and Zhou and Stansby [9]).

The first analytical study dates back to Lord Rayleigh [10], who derived the properties of bores and jumps in open channels. Probably, the first author to study the radial spread of a liquid jet over a horizontal plane was Watson [7], although earlier attempts include Kurihara [11] and Tani [12]. Essentially, Watson developed two models: the first was an inviscid model, where he assumed that the thrust of the pressure at the jump was equal to the rate at which momentum was destroyed; his second approach, a viscous model, was to use the Prandtl

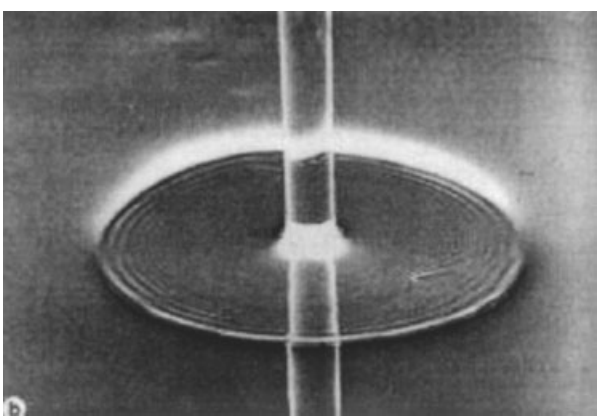

Figure 1. Example of a circular-hydraulic jump. (Reprinted with permission of Academic Press from the book *Modeling Axisymmetric Flows* by Stanley Middleman.)

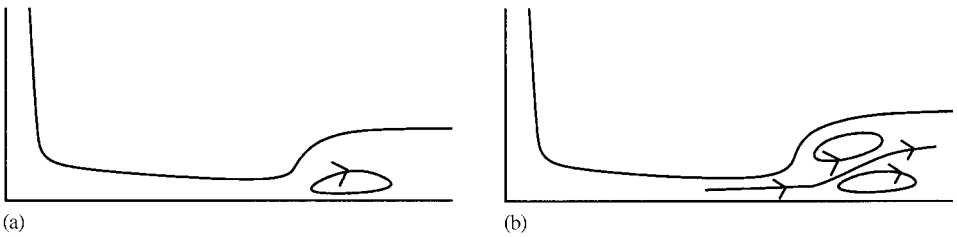

Figure 2. Types of circular-hydraulic jumps: (a) Type I; (b) Type II.

boundary layer approximation. This, he argued, was valid up until the jump when recirculation occurs and, using this theory, he established a similarity solution. Basically, Watson's two models provide estimates of the radial location of the jump. However, experimental tests have not always agreed with these models and they have been numerous [13–17]. Some of these investigations have found rough agreement with the (viscous) model, some have found good agreement for a limited range of parameters and others have found relatively poor agreement. In particular, Craik *et al.* [15] reported that Watson's model works best when the jump radius is more than 10 times the subcritical depth, with larger disagreement for smaller radii. From this and the other discrepancies between Watson's theory and the many experiments, it might be surmised that Watson's model is less accurate when the downstream flow is too deep or when the upstream-Froude number is too high.

A possible explanation for these differences may be that the flow just behind the jump can separate, creating a recirculating eddy attached to the horizontal surface (there is clear experimental evidence for this). The separation is a result of the abrupt increase in hydrostatic pressure at the jump, an effect that is clearly heightened when the downstream flow is deeper. Measurements by Craik *et al.* [15] and Errico [16] show that the separated region can be quite long and that its length changes significantly with the flow conditions. Further, the supercritical film is deflected upwards and travels over the separated region while maintaining a high speed. Clearly, a one-dimensional momentum conservation model could be affected by the complex flow field at the jump.

However, there are additional complications: it has been observed that the shape of the jump can take different forms—smooth, curved, showing standing or radiating waves, or displaying clear instability. The parameters reported to be responsible for these changes include downstream depth [15], increasing the volume flow [16, 18] and increasing upstream Froude number [14].

In recent experiments [19–21], the depth on the downstream side of the jump was controlled by varying the height of a circular wall. Experimental results show that a circular-hydraulic jump has two kinds of steady states (in addition to the unstable states alluded to above), that are reached by varying the height of the circular wall. When the wall is small, or there is no wall at all, a state with the eddy on the bottom horizontal surface is achieved as in Figure 2(a). This flow structure is called Type I. On increasing the wall height, the jump becomes steeper until a critical wall height be attained. The liquid at the jump then topples for wall heights larger than this critical value. This results in another steady state where, in addition to the eddy on the bottom horizontal line, an eddy on the surface also appears (see Figure 2(b)). This flow structure is called Type II. Further, Ellegaard *et al.* [20, 21] have

shown that, by varying the wall height when in a Type II flow regime, a circular-hydraulic jump can change into various regular polygonal shapes.

A systematic experimental programme has been carried out by Liu and Lienhard [22], in which they attempt to map out under what circumstances the jump is unstable, of Type I, or of Type II. Unfortunately, these results have all been performed at a high-Reynolds number and so a comparison with the simulated results of this paper is not yet possible at the present time.

Finally, an asymptotic high-Reynolds number analysis of the flow, around the upstream end of a laminar jump in a layer of uniform velocity with a thin viscous sublayer, was carried out by Gajjar and Smith [23] using interacting boundary layer theory. Their analysis was subsequently extended by Bowles and Smith [24] to large Froude number fully developed layers, and again by Higuera [25, 26]. Despite all this research activity, the hydraulic jump is not yet fully understood: it is, to quote Gajjar and Smith [23], clearly a complicated process.

2.1. Outline of Watson's approximate analytical solution

By examining the velocity distribution of an axisymmetric jet impinging onto a flat surface, Watson [7] developed, upstream of the jump, an approximate analytical solution based on matching two boundary layer approximations for the thickness of the fluid layer. He also obtained an analytical solution in the case of an inviscid fluid based on mass and energy conservation. In this paper, we will refer to these two solutions as VISCOUS and INVISCID, respectively. His principal results for the VISCOUS solution are now briefly discussed.

Watson considered it advantageous to divide the fluid flow into four regions; namely, (i) near to the stagnation point, where the radial distance is $r = O(a)$ and the boundary layer thickness is $\delta = O(va/U_0)^{1/2}$, with a and U_0 being, respectively, the radius and speed of the impinging jet, and v the kinematic viscosity coefficient; (ii) for $r \gg a$, where the conditions in region (i) are not important and the boundary layer is similar to the Blasius on a flat plate; (iii) from the point where the boundary layer absorbs the layer of fluid to the point where the velocity profile becomes self-similar; and (iv) at large distances from the stagnation point where the final similarity solution is valid.

According to Watson's analysis, the VISCOUS solution is valid only in regions (ii) and (iv) for the Reynolds number $R = Q/va \gg 1$, with $Q = \pi a^2 U_0$ being the volumetric rate of flow. His approximate solution is not applicable in the vicinity of the stagnation point, since the radial distance is $r \approx a$. Neglecting the transition region (iii) and using the technique of Kármán–Pohlhausen [27], he matched the solutions in region (ii) given by the Blasius profile and in region (iv) given by the velocity profile

$$u = U(r) f(z/\delta) \tag{1}$$

where $U(r)$ is the speed at the free surface and f is the similarity profile which depends on a low-order representation of the Jacobian-elliptic function (see Watson [7], p. 484).

By using the approximate velocity profile (1) in the momentum integral equation, Watson deduced the following explicit relation for the boundary layer thickness

$$r^2\delta^2 - \frac{c^3\sqrt{3}}{(\pi - c\sqrt{3})}\frac{vr^3}{U_0} = C \tag{2}$$

where $c = 1.402$ and C is an integration constant. Based on an order of magnitude analysis, he concluded that $C = O(va^3/U_0)$ in the region where $r = O(a)$, and that $C = O(a^3/r^3)$ in the region where $a \ll r < r_0$, with $r_0 = 0.3155aRe^{1/3}$ being the radial position at which the boundary layer just absorbs the flow. This integration constant was considered to be negligible by Watson and, as a result, he estimated the depth ξ of the fluid to be

$$\xi(r) = (a^2/2r) + (1 - (2\pi/3\sqrt{3}c^2))\delta \tag{3}$$

for $r < r_0$ and to be

$$\xi(r) = \frac{2\pi^2}{3\sqrt{3}} \frac{v(r^3 + l^2)}{Qr} \tag{4}$$

for $r \geqslant r_0$, where l is an arbitrary constant which was estimated by considering the initial development of the boundary layer to be $l = 0.567aR^{1/3}$.

Furthermore, applying the momentum balance and knowing the downstream film height d, regarded as prescribed by the outflow conditions, Watson derived expressions for the location $r = r_1$ at which the hydraulic jump must occur:

$$\frac{r_1 d^2 g_z a^2}{Q^2} + \frac{a^2}{2\pi^2 r_1 d} = 0.01676((r_1/a)^3 Re^{-1} + 0.1826)^{-1} \tag{5}$$

for $r_1 \geqslant r_0$ and

$$\frac{r_1 d^2 g_z d^2}{Q^2} + \frac{a^2}{2\pi^2 r_1 d} = 0.10132 - 0.1297(r_1/a)^{3/2} Re^{-1/2} \tag{6}$$

for $r_1 < r_0$, where g_z is the component of the gravitational acceleration in vertical direction z.

In Section 5 a quantitative comparison between Watson's analytical predictions and numerical results will be presented. An assessment of the error introduced in the analytical approximation will also be undertaken.

3. GOVERNING EQUATIONS AND APPROXIMATION OF THE CONVECTIVE TERMS

3.1. Basic equations

The conservation laws for time-dependent incompressible fluid flow are the Navier–Stokes equations and the continuity equation. In conservative vector form they are, respectively, written as

$$\frac{\partial \mathbf{v}}{\partial t} + \nabla \cdot (\mathbf{vv}) = -\nabla p + \frac{1}{Re} \nabla^2 \mathbf{v} + \frac{1}{Fr^2} \mathbf{g} \tag{7}$$

$$\nabla \cdot \mathbf{v} = 0 \tag{8}$$

where t is the time, $\mathbf{v}$ the velocity vector, p the kinematic pressure, $\mathbf{g}$ the gravitational acceleration, and $Re = U_0 D/v$ and $Fr = U_0/\sqrt{D|\mathbf{g}|}$ the Reynolds and Froude numbers,

respectively. The dependent variables in Equations (7) and (8) have been nondimensionalized by a characteristic velocity U_0, length scale D and reference kinematic viscosity v.

3.2. Approximation of the convective terms

It is now well established that the convective terms $\nabla \cdot (\mathbf{vv})$ in the Navier–Stokes equations are responsible for most of the complex flow phenomena. They are also the major cause of numerical difficulties: the usual CD (Central Difference) scheme may lead to unphysical oscillatory behaviour in regions of the flow where convection dominates diffusion, and thereby violating the boundedness of the solution; the classical FOU (First-Order Upwind) scheme overcomes these difficulties, but it increasingly imparts errors, so-called numerical diffusion, to the solution as the Peclét number is increased.

A number of high-order convection schemes have been developed over the years in order to reduce unphysical numerical oscillations and, at the same time, minimize the effects of artificial numerical diffusion. Early attempts were the SOU (Second-Order Upwind) scheme [28] and the use of deferred correction with central differencing [29]. Leonard [30] combined the accuracy of quadratic interpolation with stability to produce a third-order upwind scheme. However, Quadratic Upstream Interpolation for Convective Kinematics (QUICK), as Leonard's scheme was called, can introduce undershooting and overshooting in regions of high velocity gradients. To circumvent these difficulties, Gaskell and Lau [31] introduced the Sharp and Monotonic Algorithm for Realistic Transport (SMART) method. SMART has the high order of the QUICK with the advantage of boundedness, that is, the calculated velocity is never allowed below or above the minimum or maximum neighbouring velocities.

Other oscillation-free convection schemes then followed. Zhu [32] developed a second-order scheme called Hybrid-Linear Parabolic Approximation (HLPA), while Varonos and Bergeles [33] obtained a second/third-order method Variable-Order Non-Oscillatory Scheme (VONOS). This method was based on Bounded Second-Order Upwind (BSOU) of Papadakis and Bergeles [34] and the QUICK scheme. A comparison between SMART, VONOS and NOTABLE, a scheme of Pascau and Perez [35], was made using the driven-cavity problem: the results favoured the VONOS scheme.

In summary, these convection schemes can be written down as follows. Consider Figure 3 for approximating the partial derivative of a generic variable ϕ at the point P_0 say $[\partial\phi/\partial s]$, where s represents one of the independent variables x, y, or z, and ϕ_A, ϕ_B are values of the generic variable at the points P_A and P_B, respectively.

The first derivative may be approximated (for example at P_0) by the expression

$$\left.\frac{\partial\phi}{\partial s}\right|_{P_0} = \frac{\phi_B - \phi_A}{\Delta s}.$$

By using each of the schemes mentioned above, the values of ϕ_A and ϕ_B are obtained in terms of the neighbouring-grid values $\phi_{-2}, \ldots, \phi_2$ and the convective-velocity directions V_A and V_B by setting:

- **FOU**:

$$\phi_B = \begin{cases} \phi_0, & \text{if } V_B \geqslant 0 \\ \phi_1, & \text{otherwise,} \end{cases} \qquad \phi_A = \begin{cases} \phi_{-1}, & \text{if } V_A \geqslant 0 \\ \phi_0, & \text{otherwise} \end{cases}$$

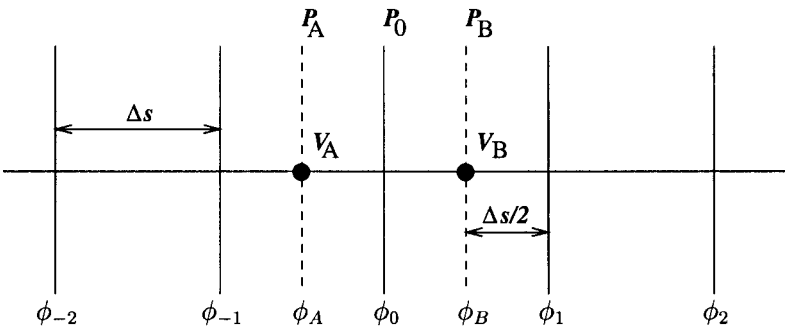

Figure 3. Stencil used for calculating ϕ_A and ϕ_B using various schemes.

- **CD**:

$$\phi_B = \frac{\phi_1 + \phi_0}{2}, \qquad \phi_A = \frac{\phi_0 + \phi_{-1}}{2}$$

- **QUICK**:

$$\phi_B = \begin{cases} \frac{3}{8}\phi_1 + \frac{6}{8}\phi_0 - \frac{1}{8}\phi_{-1}, & \text{if } V_B \geqslant 0 \\ \frac{3}{8}\phi_0 + \frac{6}{8}\phi_1 - \frac{1}{8}\phi_2, & \text{if } V_B < 0 \end{cases} \qquad \phi_A = \begin{cases} \frac{3}{8}\phi_0 + \frac{6}{8}\phi_{-1} - \frac{1}{8}\phi_{-2}, & \text{if } V_A \geqslant 0 \\ \frac{3}{8}\phi_{-1} + \frac{6}{8}\phi_0 - \frac{1}{8}\phi_1, & \text{if } V_A < 0 \end{cases}$$

- **SMART**:

$$\text{if } V_B \geqslant 0, \quad \phi_B = \begin{cases} \phi_0, & \text{if } \hat{\phi}_0 \notin [0,1] \\ 10\phi_0 - 9\phi_{-1}, & \text{if } \hat{\phi}_0 \in [0, 3/74) \\ \frac{3}{8}\phi_1 + \frac{6}{8}\phi_0 - \frac{1}{8}\phi_{-1}, & \text{if } \hat{\phi}_0 \in [3/74, 5/6) \\ \phi_1, & \text{if } \hat{\phi}_0 \in [5/6, 1] \end{cases}$$

$$\text{if } V_B < 0, \quad \phi_B = \begin{cases} \phi_1, & \text{if } \hat{\phi}_1 \notin [0,1] \\ 10\phi_1 - 9\phi_2, & \text{if } \hat{\phi}_1 \in [0, 3/74) \\ \frac{3}{8}\phi_0 + \frac{6}{8}\phi_1 - \frac{1}{8}\phi_2, & \text{if } \hat{\phi}_1 \in [3/74, 5/6) \\ \phi_0, & \text{if } \hat{\phi}_1 \in [5/6, 1] \end{cases}$$

$$\text{if } V_A \geqslant 0, \quad \phi_A = \begin{cases} \phi_{-1}, & \text{if } \hat{\phi}_{-1} \notin [0,1] \\ 10\phi_{-1} - 9\phi_{-2}, & \text{if } \hat{\phi}_{-1} \in [0, 3/74) \\ \frac{3}{8}\phi_0 + \frac{6}{8}\phi_{-1} - \frac{1}{8}\phi_{-2}, & \text{if } \hat{\phi}_{-1} \in [3/74, 5/6) \\ \phi_0, & \text{if } \hat{\phi}_{-1} \in [5/6, 1] \end{cases}$$

$$\text{if } V_A<0, \quad \phi_A=\begin{cases}\phi_0, & \text{if } \hat{\phi}_0\notin[0,1]\\ 10\phi_0-9\phi_1, & \text{if } \hat{\phi}_0\in[0,3/74)\\ \frac{3}{8}\phi_{-1}+\frac{6}{8}\phi_0-\frac{1}{8}\phi_1, & \text{if } \hat{\phi}_0\in[3/74,5/6)\\ \phi_{-1}, & \text{if } \hat{\phi}_0\in[5/6,1]\end{cases}$$

- **HLPA**:

$$\text{if } V_B\geqslant 0, \quad \phi_B=\begin{cases}\phi_0, & \text{if } \hat{\phi}_0\notin[0,1]\\ \phi_0+(\phi_1-\phi_0)\hat{\phi}_0, & \text{if } \hat{\phi}_0\in[0,1]\end{cases}$$

$$\text{if } V_B<0, \quad \phi_B=\begin{cases}\phi_1, & \text{if } \hat{\phi}_1\notin[0,1]\\ \phi_1+(\phi_0-\phi_1)\hat{\phi}_1, & \text{if } \hat{\phi}_1\in[0,1]\end{cases}$$

$$\text{if } V_A\geqslant 0, \quad \phi_A=\begin{cases}\phi_{-1}, & \text{if } \hat{\phi}_{-1}\notin[0,1]\\ \phi_{-1}+(\phi_0-\phi_{-1})\hat{\phi}_{-1}, & \text{if } \hat{\phi}_{-1}\in[0,1]\end{cases}$$

$$\text{if } V_A<0, \quad \phi_A=\begin{cases}\phi_0, & \text{if } \hat{\phi}_0\notin[0,1]\\ \phi_0+(\phi_{-1}-\phi_0)\hat{\phi}_0, & \text{if } \hat{\phi}_0\in[0,1],\end{cases}$$

- **VONOS**:

$$\text{if } V_B\geqslant 0, \quad \phi_B=\begin{cases}\phi_0, & \text{if } \hat{\phi}_0\notin[0,1]\\ 10\phi_0-9\phi_{-1}, & \text{if } \hat{\phi}_0\in[0,3/74)\\ \frac{3}{8}\phi_1+\frac{6}{8}\phi_0-\frac{1}{8}\phi_{-1}, & \text{if } \hat{\phi}_0\in[3/74,1/2)\\ 1.5\phi_0-0.5\phi_{-1}, & \text{if } \hat{\phi}_0\in[1/2,2/3)\\ \phi_1 & \text{if } \hat{\phi}_0\in[2/3,1]\end{cases}$$

$$\text{if } V_B<0, \quad \phi_B=\begin{cases}\phi_1, & \text{if } \hat{\phi}_1\notin[0,1]\\ 10\phi_1-9\phi_2, & \text{if } \hat{\phi}_1\in[0,3/74)\\ \frac{3}{8}\phi_0+\frac{6}{8}\phi_1-\frac{1}{8}\phi_2, & \text{if } \hat{\phi}_1\in[3/74,1/2)\\ 1.5\phi_1-0.5\phi_2, & \text{if } \hat{\phi}_1\in[1/2,2/3)\\ \phi_0 & \text{if } \hat{\phi}_1\in[2/3,1]\end{cases}$$

$$\text{if } V_A\geqslant 0, \quad \phi_A=\begin{cases}\phi_{-1}, & \text{if } \hat{\phi}_{-1}\notin[0,1]\\ 10\phi_{-1}-9\phi_{-2}, & \text{if } \hat{\phi}_{-1}\in[0,3/74)\\ \frac{3}{8}\phi_0+\frac{6}{8}\phi_{-1}-\frac{1}{8}\phi_{-2}, & \text{if } \hat{\phi}_{-1}\in[3/74,1/2)\\ 1.5\phi_{-1}-0.5\phi_{-2}, & \text{if } \hat{\phi}_{-1}\in[1/2,2/3)\\ \phi_0 & \text{if } \hat{\phi}_{-1}\in[2/3,1]\end{cases}$$

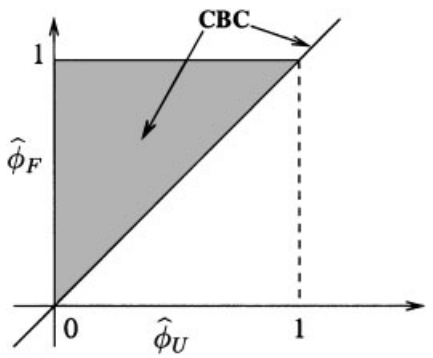

Figure 4. CBC region in the $\hat{\phi}_F - \hat{\phi}_U$ plane.

$$\text{if } V_A < 0, \quad \phi_A = \begin{cases} \phi_0, & \text{if } \hat{\phi}_0 \notin [0,1] \\ 10\phi_0 - 9\phi_1, & \text{if } \hat{\phi}_0 \in [0, 3/74) \\ \dfrac{3}{8}\phi_{-1} + \dfrac{6}{8}\phi_0 - \dfrac{1}{8}\phi_1, & \text{if } \hat{\phi}_0 \in [3/74, 1/2) \\ 1.5\phi_0 - 0.5\phi_1, & \text{if } \hat{\phi}_0 \in [1/2, 2/3) \\ \phi_{-1}, & \text{if } \hat{\phi}_0 \in [2/3, 1] \end{cases}$$

The expressions for $\hat{\phi}_U$, $(U = -1, 0, 1)$, appearing in the SMART, HLPA and VONOS schemes, are defined by the normalized variable formulation of Leonard [30] as

$$\hat{\phi}_U = \frac{\phi_U - \phi_R}{\phi_D - \phi_R} \tag{9}$$

where the downstream, upstream, and remote-upstream neighbouring nodes, labelled respectively as D, U and R, are taken relative to the point F $(F = A, B)$, according to the convective-velocity direction there. For example, consider the point A between nodes -1 and 0 as shown in Figure 3, and assume that the velocity at this point is greater than zero $(V_A > 0)$. Then, relative to this point, the neighbouring nodes D, U and R would correspond to the nodes 0, -1 and -2, respectively.

It should be pointed out that, based on the local direction of flow, the concept of variable normalization proposed by Leonard and his monotonicity criterion constitute the basis on which high-order oscillation-free convection schemes are constructed. If at most three neighbouring nodal values are used to approximate point values, such as those appearing in Equation (9), then a necessary and sufficient condition for guaranteeing a bounded solution is the Convection Boundedness Criterion (CBC), formulated by Gaskell and Lau [31]. In this context, the four schemes FOU, SMART, HLPA and VONOS unconditionally satisfy the CBC, while the schemes CD and QUICK only conditionally satisfy the CBC. The CBC is illustrated in Figure 4, where the line $\hat{\phi}_F = \hat{\phi}_U$ and the shaded area form the region over which it is valid.

4. AXISYMMETRIC NAVIER–STOKES EQUATION

4.1. Brief description of the axisymmetric GENSMAC code

The axisymmetric GENSMAC code [1] solves the Navier–Stokes equations and the continuity equation for an incompressible-viscous fluid (Equations (7) and (8)). It is an updated version of the SMAC method [6] for calculating time-dependent free-surface flow, employing pressure and velocity as the primary dependent variables. It uses a finite-difference approach on a staggered grid. An adaptive time-stepping technique has been implemented and a conjugate-gradient solver is employed to solve the discrete Poisson equation. The code is designed to deal with moving free-surface flows within a general domain containing free-slip and/or no-slip rigid boundaries.

4.1.1. Basic equations. In cylindrical coordinates, Equations (7) and (8) may be expressed in conservative form as

$$\frac{\partial u}{\partial t}+\frac{1}{r}\frac{\partial(ruu)}{\partial r}+\frac{\partial(uv)}{\partial z}=-\frac{\partial p}{\partial r}+\frac{1}{Re}\frac{\partial}{\partial z}\left(\frac{\partial u}{\partial z}-\frac{\partial v}{\partial r}\right)+\frac{1}{Fr^2}g_r, \tag{10}$$

$$\frac{\partial v}{\partial t}+\frac{1}{r}\frac{\partial(ruv)}{\partial r}+\frac{\partial(vv)}{\partial z}=-\frac{\partial p}{\partial z}-\frac{1}{Re}\frac{1}{r}\frac{\partial}{\partial r}\left(r\left(\frac{\partial u}{\partial z}-\frac{\partial v}{\partial r}\right)\right)+\frac{1}{Fr^2}g_z \tag{11}$$

$$\frac{1}{r}\frac{\partial(ru)}{\partial r}+\frac{\partial v}{\partial z}=0 \tag{12}$$

where u and v are, respectively, the radial and vertical components of the velocity field. All other variables and parameters were previously defined. Full details of the axisymmetric GENSMAC code have recently appeared in Reference [1], and the reader is referred to this article. However, for continuity in this paper, we provide an outline of the boundary conditions and solution procedure.

4.1.2. Boundary conditions. Boundary conditions must be imposed on fixed boundaries and free surfaces. On fixed boundaries, we can impose no-slip, free-slip, prescribed inflow, prescribed outflow and continuative outflow (for details, see Tomé and McKee [4], Amsden and Harlow [6]). The implementation of these boundary conditions is performed in the same way as in the GENSMAC code. The appropriate free-surface boundary conditions are the vanishing of the normal and tangential stresses which, in the absence of surface tension, are [36]

$$\mathbf{n}\cdot\sigma\cdot\mathbf{n}=0 \tag{13}$$

$$\mathbf{m}\cdot\sigma\cdot\mathbf{n}=0 \tag{14}$$

where $\mathbf{n}$ and $\mathbf{m}$ are, respectively, local-unit normal and tangential vectors, and σ is the stress tensor given by

$$\sigma_{ij}=-p\delta_{ij}+\frac{2}{Re}\left(\frac{\partial v_i}{\partial x_j}+\frac{\partial v_j}{\partial x_i}\right)$$

These conditions are applied by making accurate local finite-difference approximations on the free surface. Details of the application of the stress conditions are given in Tomé and McKee [4]. The appropriate boundary conditions for the Poisson equation (18) are homogeneous Dirichlet-type on the free surface and homogeneous Neumann-type on fixed boundaries.

4.1.3. Solution procedure. In order to solve Equations (10)–(12), we employ the GENSMAC methodology. In particular, when calculating $\tilde{\mathbf{u}}(r,z,t)$ in step 2, we employ an adaptive time stepping routine. It is supposed that, at a given time $t=t_0$, the solenoidal-velocity field $\mathbf{u}(r,z,t_0)$ is known and suitable boundary conditions for the velocity and pressure are given. The updated velocity field $\mathbf{u}(r,z,t)$, at $t=t_0+\delta t$, is calculated as follows:

1. Let $\tilde{p}(r,z,t)$ be an arbitrary pressure field, which satisfies the correct pressure condition on the free surface. This pressure field is constructed employing the normal-stress condition (13) at the free-surface cells, and it is chosen arbitrarily (for instance $\tilde{p}(r,z,t)=0$) at the interior cells;
2. Calculate the intermediate velocity field $\tilde{\mathbf{u}}(r,z,t)$ from the explicitly discretised form of

$$\frac{\partial \tilde{u}}{\partial t}=\left[-\frac{1}{r}\frac{\partial(ruu)}{\partial r}-\frac{\partial(uv)}{\partial z}-\frac{\partial \tilde{p}}{\partial r}+\frac{1}{Re}\frac{\partial}{\partial z}\left(\frac{\partial u}{\partial z}-\frac{\partial v}{\partial r}\right)+\frac{1}{Fr^2}g_r\right]_{t=t_0} \tag{15}$$

$$\frac{\partial \tilde{v}}{\partial t}=\left[-\frac{1}{r}\frac{\partial(ruv)}{\partial r}-\frac{\partial(vv)}{\partial z}-\frac{\partial \tilde{p}}{\partial z}-\frac{1}{Re}\frac{1}{r}\frac{\partial}{\partial r}\left(r\left(\frac{\partial u}{\partial z}-\frac{\partial v}{\partial r}\right)\right)+\frac{1}{Fr^2}g_z\right]_{t=t_0} \tag{16}$$

   with $\tilde{\mathbf{u}}(r,z,t_0)=\mathbf{u}(r,z,t_0)$, using the correct boundary conditions for $\mathbf{u}(r,z,t_0)$. It can be shown that $\tilde{\mathbf{u}}(r,z,t)$ possesses the correct vorticity at time t. However, $\tilde{\mathbf{u}}(r,z,t)$ does not satisfy Equation (12), in general. Let

$$\mathbf{u}(r,z,t)=\tilde{\mathbf{u}}(r,z,t)-\nabla\psi(r,z,t) \tag{17}$$

   with ψ an auxiliary potential field such that

$$\nabla^2\psi(r,z,t)=\nabla\cdot\tilde{\mathbf{u}}(r,z,t). \tag{18}$$

   Thus, $\mathbf{u}(r,z,t)$ now satisfies Equation (12) and the vorticity remains unchanged. Therefore, $\mathbf{u}(r,z,t)$ is identified as the updated velocity field at time t;
3. Solve the Poisson equation (18);
4. Compute the velocity field (17);
5. Compute the pressure. It can be shown that the pressure is given by

$$p(r,z,t)=\tilde{p}(r,z,t)+\psi(r,z,t)/\delta t \tag{19}$$

6. Update the positions of the marker particles.

The last step in the calculation involves moving the marker particles to their new positions. These are virtual particles (without mass, volume, or other properties), whose coordinates are stored and updated at the end of each cycle by solving the ordinary differential equations

$$\frac{\mathrm{d}r}{\mathrm{d}t}=u, \qquad \frac{\mathrm{d}z}{\mathrm{d}t}=v$$

by Euler's method. This provides a particle with its new coordinates, allowing us to determine whether or not it has moved into a new computational cell, or if it has left the containment region through an outflow-boundary.

In Equations (15) and (16), the viscous terms and the pressure gradient are approximated using standard second-order finite differences, while the temporal derivative is discretized using a forward difference. However, the convective terms will be approximated by the various high-order upwind schemes presented in Section 3. The Poisson equation (18) is discretized using the usual five-point Laplacian operator, and the corresponding symmetric-positive definite linear system is solved by the conjugate-gradient method (e.g. Ortega [37]).

5. NUMERICAL RESULTS OF THE AXISYMMETRIC CODE

The purpose of this section is three-fold. First, we wish to demonstrate that certain known complex features of the circular-hydraulic jump are capable of being resolved. In particular, we exhibit Type I and II flows with the single and double roller, respectively. This not only provides partial validation of the code (it has, of course, been substantially validated in an earlier paper [1] but also, for the first time, demonstrates that a proper simulation of these features is possible. Secondly, we wish to compare numerical solutions obtained with the approximate analytic results of Watson [7] where appropriate. Finally, we wish to compare the different convective approximations against Watson's solution and thereby attempt to say which are acceptable and which are not.

The convective schemes of Section 3 have been implemented in the axisymmetric GENS-MAC code. We shall consider a vertical jet impinging onto a flat surface and spreading out into a thin film flowing radially away from the stagnation point (see Figure 5). The following input data are employed.

(i) **Circular hydraulic jump of Type I:**

- Domain dimensions: $0.05\,\mathrm{m} \times 0.03\,\mathrm{m}$; Inlet diameter (D): $0.008\,\mathrm{m}$;
- Inlet velocity (U_0): $0.375\,\mathrm{ms}^{-1}$; Gravitational constant (g): $9.81\,\mathrm{ms}^{-2}$;
- Kinematic viscosity (v): $1.2 \times 10^{-5}\ \mathrm{m}^2\mathrm{s}^{-1}$; Scaling parameters: $\mathrm{D} = 0.008$ m, $U_0 = 0.375\,\mathrm{ms}^{-1}$;

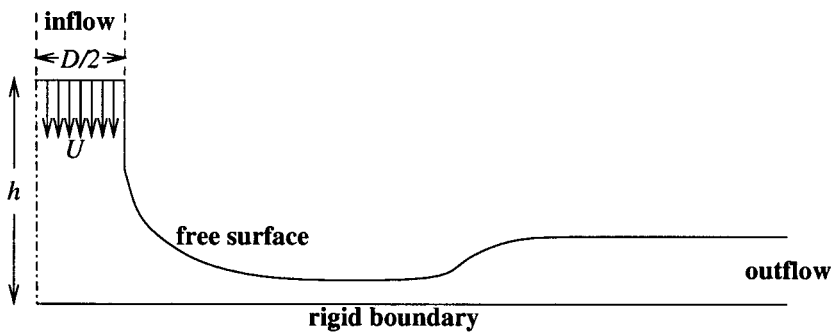

Figure 5. Flow description for an impinging jet simulation.

- Reynolds number ($Re = U_0 D/\nu$): 250; Froude number ($Fr = U_0/\sqrt{gD}$): 1.3386;
- Height of the inflow above the flat surface (h): 0.03 m.

(ii) **Circular hydraulic jump of Type II:**

- Domain dimensions: $0.05\,\mathrm{m} \times 0.03\,\mathrm{m}$; Inlet diameter (D): 0.008 m;
- Inlet velocity (U_0): $0.375\,\mathrm{ms}^{-1}$; Gravitational constant (g): $9.81\,\mathrm{ms}^{-2}$;
- Kinematic viscosity (ν): $3.75 \times 10^{-6}\ \mathrm{m}^2\ \mathrm{s}^{-1}$; Scaling parameters: $\mathrm{D} = 0.008$ m, $U_0 = 0.375\,\mathrm{ms}^{-1}$;
- Reynolds number ($Re = U_0 D/\nu$): 800; Froude number ($Fr = U_0/\sqrt{gD}$): 1.3386;
- Height of the inflow above the flat surface (h): 0.03 m.

Figure 6 shows the results of the hydraulic jump simulation using the VONOS implementation for two different choices of Reynolds number. Figure 6(a) displays the result of Type I flow and Figure 6(b) corresponds to the Type II flow.

In this figure, the curve represents the free surface, while the arrows indicate the direction of the velocity vectors. One can see from Figure 6 that the results obtained by the axisymmetric GENSMAC code display the flow structures appearing in Figure 2. In particular, Figure 6(a) shows the existence of separating rotational flow formed on the bottom interface in conjunction with the jump. Moreover, this recirculation region is, qualitatively, in accordance with experimental results of Tani [12], Craik *et al.* [15] and Bowles and Smith [24].

In order to effect a comparison with Watson's approximate analytic solution, we consider the same input data as for a Type II jump, except for the inlet velocity U_0 and the coefficient of viscosity ν. In this problem, $U_0 = 1\,\mathrm{ms}^{-1}$ and $\nu = 10^{-5}\,\mathrm{m}^2\,\mathrm{s}^{-1}$. The Froude number ($Fr = 3.5696$), based on the inlet velocity and inlet diameter, is chosen to be sufficiently large to prevent the formation of a hydraulic jump before the jet reaches the outflow-boundary. The numerical solutions are then compared to the analytic solutions given by Watson [7].

The axisymmetric GENSMAC code was run on this problem, until the jet reached the outflow-boundary. Two runs were performed for each of the convective approximations. For the first run, a mesh size of 100×60 cells ($\delta r = \delta z = 5.0 \times 10^{-3}$ m), known hereafter as Mesh I, was employed while in the second run was used a mesh size of 200×120 cells ($\delta r = \delta z = 2.5 \times 10^{-3}\,\mathrm{m}$); this will be referred to as Mesh II. Figure 7 displays the fluid surface at time $t = 8.0\,\mathrm{s}$ for Mesh II using the various convective implementations, including the FOU. It can be observed, from this figure, that QUICK, SMART, VONOS and HLPA gave similar results, while the FOU produced a much thicker jet due to its intrinsic artificial–numerical dissipation.

A comparison was then made between the surface height, obtained from the numerical solution, and the VISCOUS (Equations (3) and (4)) and INVISCID solutions; this is displayed in Figure 8. The numerical results were calculated on Mesh II using the upwind schemes QUICK, SMART, VONOS, HLPA and FOU. We restricted the analysis to the region $0.2 < (r/a)R^{-1/3} < 1.0$ (where $R = \pi a U_0/\nu = \pi Re/2 \approx 1,257$) because of the restriction $r \gg a$ and the presence of the outflow-boundary which is close to $(r/a)R^{-1/3} = 1.0$. It can be seen from Figure 8(a)–(d) that the results obtained using QUICK, SMART, VONOS and HLPA are very similar, showing a small difference when compared to the VISCOUS solution. We believe that most of this difference may be attributed to the approximations made in obtaining

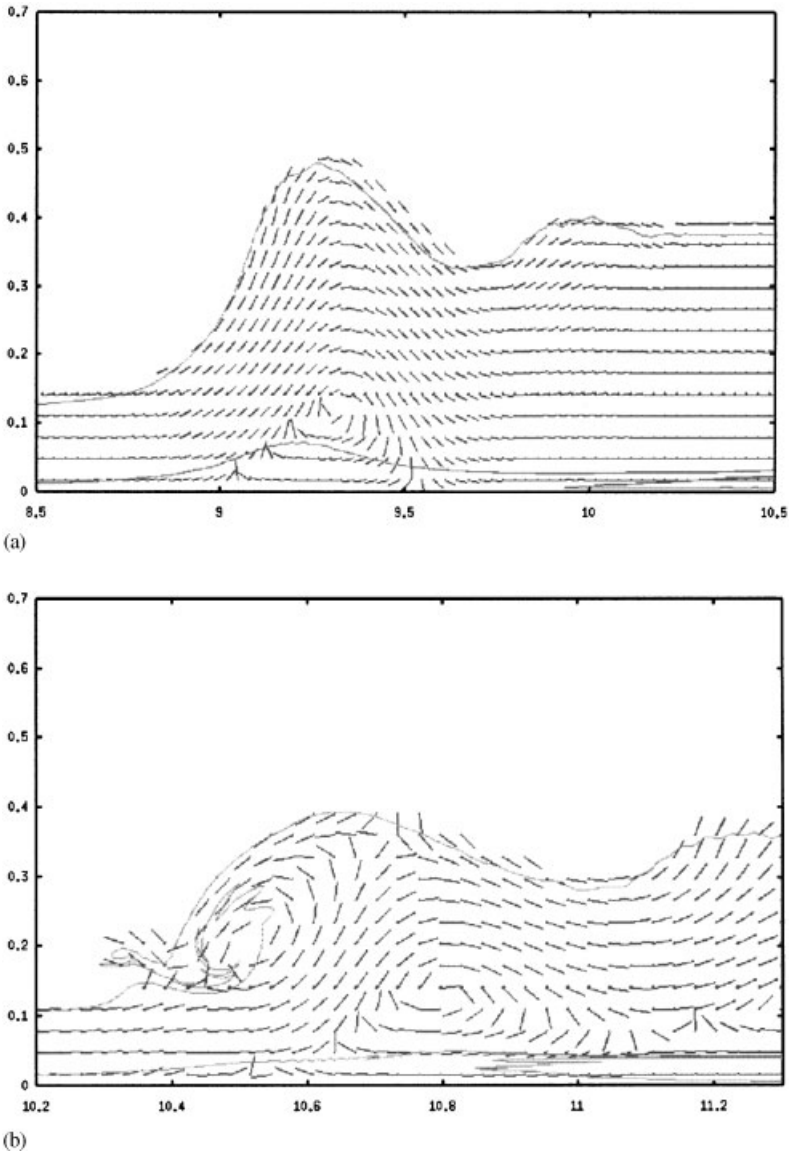

Figure 6. Results of the numerical simulation of the hydraulic jumps using the VONOS scheme, showing fluid surface (curve) and velocity vectors (arrows): (a) Type I (single roller, $Re = 250$); (b) Type II (double roller, $Re = 800$).

the VISCOUS solution. In fact, when the grid was refined, with a mesh size of 400×240 cells (Mesh III, $\delta z = \delta r = 1.25 \times 10^{-4}$ m), the numerical solution converged to a solution close to that obtained with Mesh II for the four schemes. Figure 8(f) shows the numerical solution in the three meshes using the HLPA scheme. We point out that the FOU solution on Mesh II

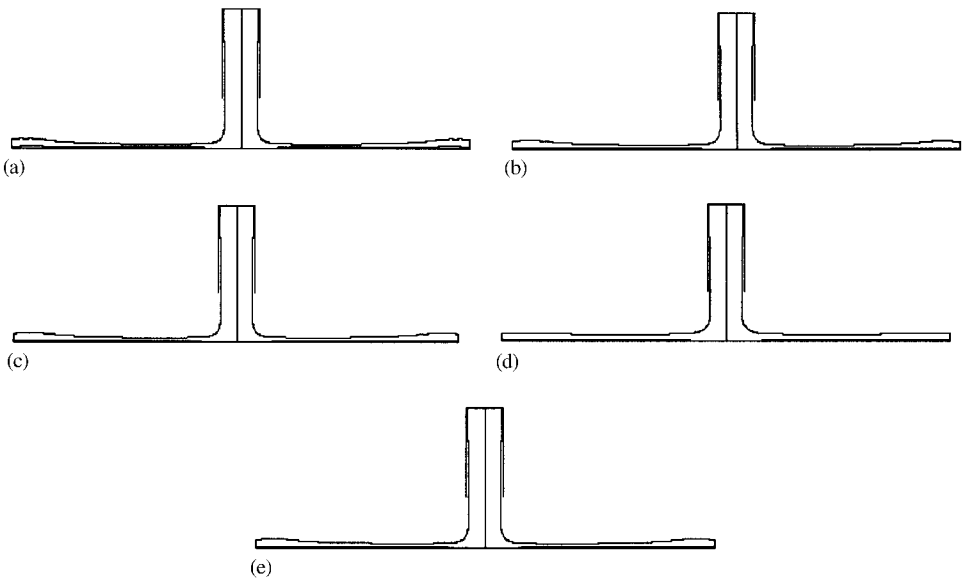

Figure 7. Jet surface at time $t = 8.0$ s using the various convection approximations on Mesh II: (a) QUICK; (b) VONOS; (c) SMART; (d) FOU; (e) HLPA.

(Figure 8(e)) deviates considerably from the VISCOUS solution, with a behaviour that veers away from that of the INVISCID curve as $(r/a)R^{-1/3}$ increases. The thickness of the fluid layer due to FOU solution is much greater than that of the analytical solution on most of the region of interest. This we attribute to the fact that the FOU solution introduces considerable artificial–numerical viscosity.

A quantitative analysis, using the l_2 norm, of the error between the numerical solutions and VISCOUS solution, for Meshes I, II and III, is summarized in Table I. These results quantify the observations regarding Figure 8. Again, QUICK, SMART, VONOS and HLPA show very similar results with a relatively small error; QUICK and HLPA giving the best results on Mesh II, and SMART and VONOS giving the best results on Mesh III. The classical FOU shows a much larger error on Meshes II and III. Surprisingly, the FOU results for Mesh I are somewhat better when compared with those of Meshes II and III. Nevertheless, they are much worse than that ones obtained by the other convection schemes.

The discrepancy between the approximate analytical solution, developed by Watson, and the numerical solution, obtained by axisymmetric GENSMAC code, can be seen by using the explicit relation (2) for the boundary layer thickness. Figure 9(a) shows the behaviour of the boundary layer thicknesses derived by Watson (WATSON) and that obtained using the GENSMAC code (GENSMAC) with the VONOS scheme on Mesh II. From this figure, it is clear that the axisymmetric GENSMAC code correctly predicts the boundary layer growth far from the stagnation point ($(r/a)R^{-1/3} > 0.2$). Figure 9(b) displays the error distribution ($C = C((r/a)R^{-1/3})$) given by Equation (2). It is from this figure that the disagreement between theory and numerics may be attributed to the fact that Watson neglects the integration constant C everywhere in his approximate analytical solution.

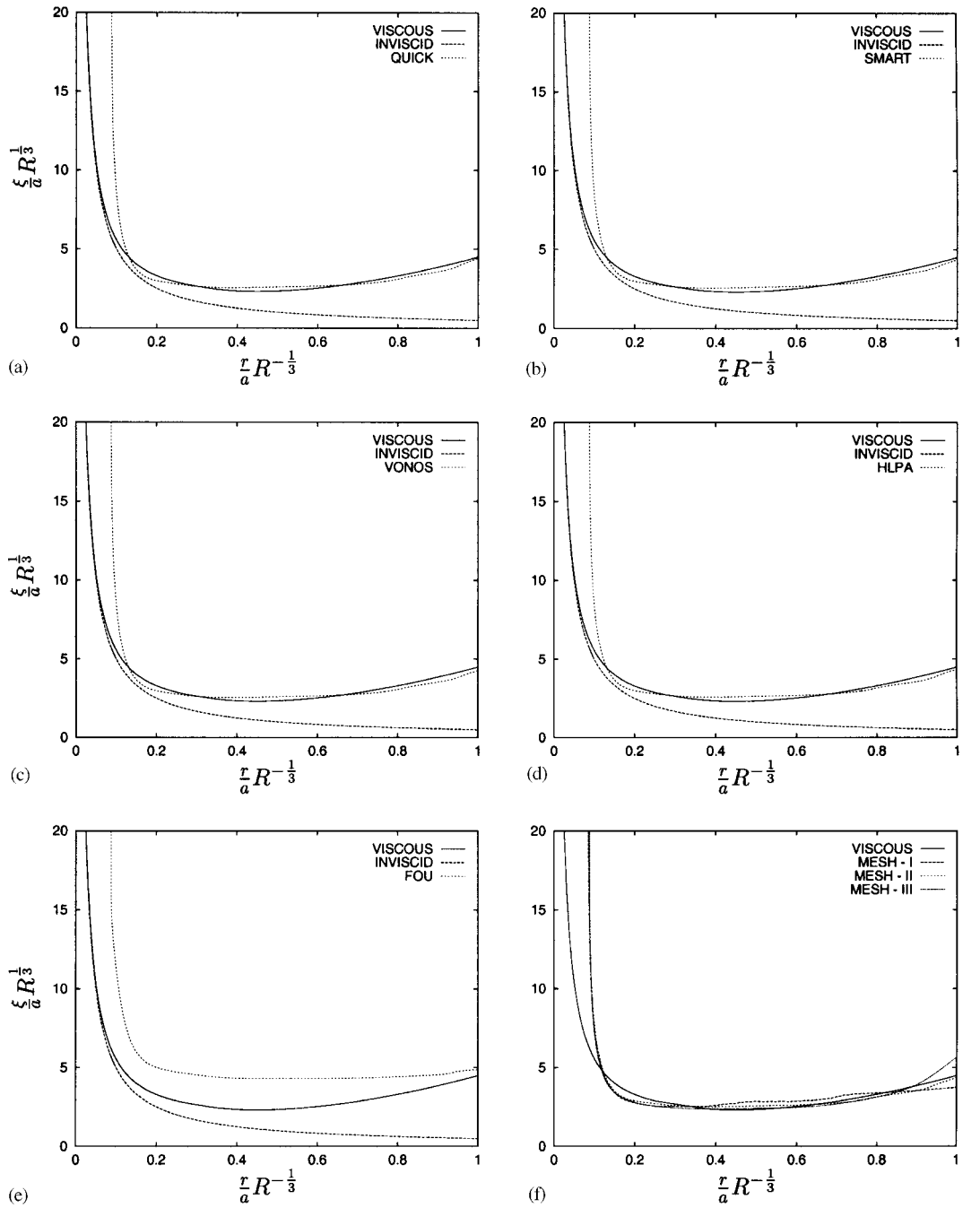

Figure 8. Comparison between the numerical (axisymmetric GENSMAC code) and approximate analytic solutions (Watson): (a)–(e) show the comparisons using various upwind schemes on Mesh II; (f) shows the numerical solution using the HLPA scheme on Meshes I, II and III.

Table I. Normalized l_2-errors in the surface height ($\|\xi_{\text{VISCOUS}} - \xi_{\text{Numerical}}\|_2)/\|\xi_{\text{VISCOUS}}\|_2$).

Mesh	QUICK	SMART	VONOS	HLPA	FOU
I (100×60)	0.2181066	0.2181084	0.2116055	0.2121379	0.3260995
II (200×120)	0.0609543	0.0622931	0.0704282	0.0613914	0.4621081
III (400×240)	0.0554971	0.0510175	0.0499362	0.0521920	0.3911262

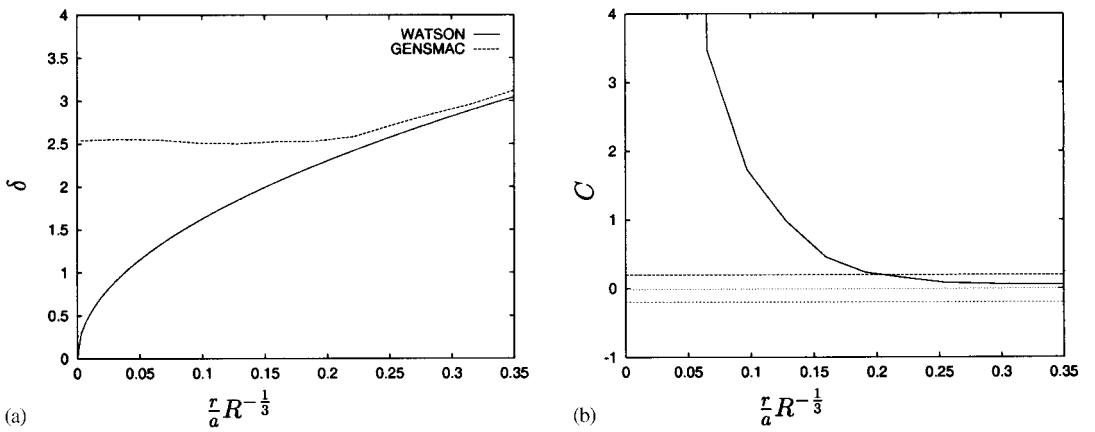

Figure 9. (a) Boundary-layer thickness obtained by Watson (WATSON) and GENSMAC code (GENSMAC); (b) Watson's error distribution.

6. 3D NAVIER–STOKES EQUATION

6.1. Basic equations and method of solution

6.1.1. Basic equations. In three-dimensional Cartesian coordinates, Equations (7) and (8) may be written as

$$\frac{\partial u}{\partial t} + \frac{\partial (uu)}{\partial x} + \frac{\partial (vu)}{\partial y} + \frac{\partial (wu)}{\partial z} = -\frac{\partial p}{\partial x} + \frac{1}{Re}\left[\frac{\partial^2 u}{\partial x^2} + \frac{\partial^2 u}{\partial y^2} + \frac{\partial^2 u}{\partial z^2}\right] + \frac{1}{Fr^2} g_x \tag{20}$$

$$\frac{\partial v}{\partial t} + \frac{\partial (uv)}{\partial x} + \frac{\partial (vv)}{\partial y} + \frac{\partial (wv)}{\partial z} = -\frac{\partial p}{\partial y} + \frac{1}{Re}\left[\frac{\partial^2 v}{\partial x^2} + \frac{\partial^2 v}{\partial y^2} + \frac{\partial^2 v}{\partial z^2}\right] + \frac{1}{Fr^2} g_y \tag{21}$$

$$\frac{\partial w}{\partial t} + \frac{\partial (uw)}{\partial x} + \frac{\partial (vw)}{\partial y} + \frac{\partial (ww)}{\partial z} = -\frac{\partial p}{\partial z} + \frac{1}{Re}\left[\frac{\partial^2 w}{\partial x^2} + \frac{\partial^2 w}{\partial y^2} + \frac{\partial^2 w}{\partial z^2}\right] + \frac{1}{Fr^2} g_z \tag{22}$$

$$\frac{\partial u}{\partial x} + \frac{\partial v}{\partial y} + \frac{\partial w}{\partial z} = 0 \tag{23}$$

where all variables and parameters have been defined previously.

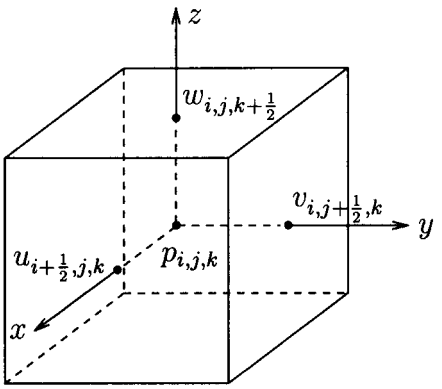

Figure 10. Typical cell showing the location of the dependent variables.

The method of solution is essentially the same as that given in Section 4 for axisymmetric flows. A full description, especially on how to implement the boundary conditions, can be found in Castelo *et al.* [2] or Tomé *et al.* [3].

6.1.2. Discretization. It is helpful and probably necessary to provide a description of how the convective terms are dealt with. Firstly, to solve the explicit discretization of Equations (20)–(22) we employ, as before, a finite difference method on a staggered grid; a typical cell showing the physical locations at which the dependent variables are defined is illustrated in Figure 10. The convective-transport terms are approximated using the various differencing schemes presented in Section 3. Thus, the discretized versions of Equations (20)–(22) and Poisson equation (18) are, respectively, given by

$$\bar{u}_{i+\frac{1}{2},j,k} = u_{i+\frac{1}{2},j,k} - \delta t \left[\mathrm{CONV}(u)_{i+\frac{1}{2},j,k} + \frac{\tilde{p}_{i+1,j,k} - \tilde{p}_{i,j,k}}{\delta x} + \frac{1}{Fr^2} g_x \right.$$
$$+ \frac{1}{Re} \left(\frac{u_{i-\frac{1}{2},j,k} - 2u_{i+\frac{1}{2},j,k} + u_{i+\frac{3}{2},j,k}}{\delta x^2} + \frac{u_{i+\frac{1}{2},j-1,k} - 2u_{i+\frac{1}{2},j,k} + u_{i+\frac{1}{2},j+1,k}}{\delta y^2} \right.$$
$$\left. \left. + \frac{u_{i+\frac{1}{2},j,k-1} - 2u_{i+\frac{1}{2},j,k} + u_{i+\frac{1}{2},j,k+1}}{\delta z^2} \right) \right] \tag{24}$$

$$\tilde{v}_{i,j+\frac{1}{2},k} = v_{i,j+\frac{1}{2},k} - \delta t \left[\mathrm{CONV}(v)_{i,j+\frac{1}{2},k} + \frac{\tilde{p}_{i,j+1,k} - \tilde{p}_{i,j,k}}{\delta y} + \frac{1}{Fr^2} g_y \right.$$
$$+ \frac{1}{Re} \left(\frac{v_{i-1,j+\frac{1}{2},k} - 2v_{i,j+\frac{1}{2},k} + v_{i+1,j+\frac{1}{2},k}}{\delta x^2} + \frac{v_{i,j-\frac{1}{2},k} - 2v_{i,j+\frac{1}{2},k} + v_{i,j+\frac{3}{2},k}}{\delta y^2} \right.$$

$$+\frac{v_{i,j+\frac{1}{2},k-1}-2v_{i,j+\frac{1}{2},k}+v_{i,j+\frac{1}{2},k+1}}{\delta z^2}\Bigg)\Bigg] \tag{25}$$

$$\tilde{w}_{i,j,k+\frac{1}{2}}=w_{i,j,k+\frac{1}{2}}-\delta t\left[\mathrm{CONV}(w)_{i,j,k+\frac{1}{2}}+\frac{\tilde{p}_{i,j,k+1}-\tilde{p}_{i,j,k}}{\delta z}+\frac{1}{Fr^2}g_z\right.$$
$$+\frac{1}{Re}\left(\frac{w_{i-1,j,k+\frac{1}{2}}-2w_{i,j,k+\frac{1}{2}}+w_{i+1,j,k+\frac{1}{2}}}{\delta x^2}+\frac{w_{i,j-1,k+\frac{1}{2}}-2w_{i,j,k+\frac{1}{2}}+w_{i,j+1,k+\frac{1}{2}}}{\delta y^2}\right.$$
$$\left.\left.+\frac{w_{i,j,k-\frac{1}{2}}-2w_{i,j,k+\frac{1}{2}}w_{i,j,k+\frac{3}{2}}}{\delta z^2}\right)\right] \tag{26}$$

$$\frac{\psi_{i+1,j,k}-2\psi_{i,j,k}+\psi_{i-1,j,k}}{\delta x^2}+\frac{\psi_{i,j+1,k}-2\psi_{i,j,k}+\psi_{i,j-1,k}}{\delta y^2}+\frac{\psi_{i,j,k+1}-2\psi_{i,j,k}+\psi_{i,j,k-1}}{\delta z^2}$$
$$=\frac{\tilde{u}_{i+\frac{1}{2},j,k}-\tilde{u}_{i-\frac{1}{2},j,k}}{\delta x}+\frac{\tilde{v}_{i,j+\frac{1}{2},k}-\tilde{v}_{i,j-\frac{1}{2},k}}{\delta y}+\frac{\tilde{w}_{i,j,k+\frac{1}{2}}-\tilde{w}_{i,j,k-\frac{1}{2}}}{\delta z} \tag{27}$$

In Equations (24)–(26), CONV(ϕ), $\phi=u$, v or w, represents the convective terms evaluated at appropriate grid nodes. The finite-difference approximations for these terms will be given in the next sub-section.

6.1.3. Finite-difference approximation of the convective terms. We now consider the application of the various convection schemes to three-dimensional flows. For brevity, only the discretization of the convective terms in the x-momentum equation is given; the other two momentum components are treated similarly.

At the node $(i+(1/2),j,k)$, the convective term CONV(u) can be written as

$$\left[\frac{\partial(uu)}{\partial x}+\frac{\partial(vu)}{\partial y}+\frac{\partial(wu)}{\partial z}\right]_{i+\frac{1}{2},j,k}=\left.\frac{\partial(uu)}{\partial x}\right|_{i+\frac{1}{2},j,k}+\left.\frac{\partial(vu)}{\partial y}\right|_{i+\frac{1}{2},j,k}+\left.\frac{\partial(wu)}{\partial z}\right|_{i+\frac{1}{2},j,k} \tag{28}$$

where the derivatives are approximated by

$$\left.\frac{\partial(uu)}{\partial x}\right|_{i+\frac{1}{2},j,k}=(\bar{u}_{i+1,j,k}u_{i+1,j,k}-\bar{u}_{i,j,k}u_{i,j,k})/\delta x \tag{29}$$

$$\left.\frac{\partial(vu)}{\partial y}\right|_{i+\frac{1}{2},j,k}=\left(\bar{v}_{i+\frac{1}{2},j+\frac{1}{2},k}u_{i+\frac{1}{2},j+\frac{1}{2},k}-\bar{v}_{i+\frac{1}{2},j-\frac{1}{2},k}u_{i+\frac{1}{2},j-\frac{1}{2},k}\right)/\delta y \tag{30}$$

$$\left.\frac{\partial(wu)}{\partial z}\right|_{i+\frac{1}{2},j,k}=\left(\bar{w}_{i+\frac{1}{2},j,k+\frac{1}{2}}u_{i+\frac{1}{2},j,k+\frac{1}{2}}-\bar{w}_{i+\frac{1}{2},j,k-\frac{1}{2}}u_{i+\frac{1}{2},j,k-\frac{1}{2}}\right)/\delta z \tag{31}$$

The convective velocities appearing in Equations (29)–(31) are obtained by averaging; namely,

$$\bar{u}_{i,j,k} = 0.5\left(u_{i+\frac{1}{2},j,k} + u_{i-\frac{1}{2},j,k}\right), \quad \bar{u}_{i+1,j,k} = 0.5\left(u_{i+\frac{3}{2},j,k} + u_{i+\frac{1}{2},j,k}\right)$$

$$\bar{v}_{i+\frac{1}{2},j+\frac{1}{2},k} = 0.5\left(v_{i,j+\frac{1}{2},k} + v_{i+1,j+\frac{1}{2},k}\right), \quad \bar{v}_{i+\frac{1}{2},j-\frac{1}{2},k} = 0.5\left(v_{i,j-\frac{1}{2},k} + v_{i+1,j-\frac{1}{2},k}\right)$$

$$\bar{w}_{i+\frac{1}{2},j,k+\frac{1}{2}} = 0.5\left(w_{i,j,k+\frac{1}{2}} + w_{i+1,j,k+\frac{1}{2}}\right), \quad \bar{w}_{i+\frac{1}{2},j,k-\frac{1}{2}} = 0.5\left(w_{i,j,k-\frac{1}{2}} + w_{i+1,j,k-\frac{1}{2}}\right)$$

We shall present the finite-difference equations for computing the first derivative in Equation (29). The corresponding difference equations for calculating the other derivatives in Equations (30) and (31) are again obtained similarly. Firstly, let us define the parameters

$$S_{i+1,j,k} = \begin{cases} 0, & \text{if } \bar{u}_{i+1,j,k} \geqslant 0 \\ 1, & \text{otherwise,} \end{cases} \quad \text{and} \quad S_{i,j,k} = \begin{cases} 0, & \text{if } \bar{u}_{i,j,k} \geqslant 0 \\ 1, & \text{otherwise} \end{cases} \tag{32}$$

Then, the velocities $u_{i,j,k}$ and $u_{i+1,j,k}$ appearing in Equation (29) can be obtained by the following convection approximations:

FOU:

$$u_{i+1,j,k} = (1 - S_{i+1,j,k})u_{i+\frac{1}{2},j,k} + S_{i+1,j,k}u_{i+\frac{3}{2},j,k}$$

$$u_{i,j,k} = (1 - S_{i,j,k})u_{i-\frac{1}{2},j,k} + S_{i,j,k}u_{i+\frac{1}{2},j,k}$$

CD:

$$u_{i+1,j,k} = \frac{u_{i+\frac{1}{2},j,k} + u_{i+\frac{3}{2},j,k}}{2}$$

$$u_{i,j,k} = \frac{u_{i-\frac{1}{2},j,k} + u_{i+\frac{1}{2},j,k}}{2}$$

QUICK:

$$u_{i+1,j,k} = (1 - S_{i+1,j,k})\left(\frac{3u_{i+\frac{3}{2},j,k} + 6u_{i+\frac{1}{2},j,k} - u_{i-\frac{1}{2},j,k}}{8}\right)$$

$$+ S_{i+1,j,k}\left(\frac{3u_{i+\frac{1}{2},j,k} + 6u_{i+\frac{3}{2},j,k} - u_{i+\frac{5}{2},j,k}}{8}\right)$$

$$u_{i,j,k} = (1 - S_{i,j,k}) \left(\frac{3u_{i+\frac{1}{2},j,k} + 6u_{i-\frac{1}{2},j,k} - u_{i-\frac{3}{2},j,k}}{8} \right) + S_{i,j,k} \left(\frac{3u_{i-\frac{1}{2},j,k} + 6u_{i+\frac{1}{2},j,k} - u_{i+\frac{3}{2},j,k}}{8} \right)$$

HLPA:

$$\hat{\phi}_{i+1,j,k} = (1 - S_{i+1,j,k}) \left(\frac{\left(u_{i+\frac{1}{2},j,k} - u_{i-\frac{1}{2},j,k} \right)}{\left(u_{i+\frac{3}{2},j,k} - u_{i-\frac{1}{2},j,k} \right)} \right) + S_{i+1,j,k} \left(\frac{\left(u_{i+\frac{3}{2},j,k} - u_{i+\frac{5}{2},j,k} \right)}{\left(u_{i+\frac{1}{2},j,k} - u_{i+\frac{5}{2},j,k} \right)} \right)$$

$$u_{i+1,j,k} = (1 - S_{i+1,j,k}) \begin{Bmatrix} u_{i+\frac{1}{2},j,k}, & \text{if } \hat{\phi}_{i+1,j,k} \notin [0,1] \\ u_{i+\frac{1}{2},j,k} + (u_{i+\frac{3}{2},j,k} - u_{i+\frac{1}{2},j,k})\hat{\phi}_{i+1,j,k}, & \text{if } \hat{\phi}_{i+1,j,k} \in [0,1] \end{Bmatrix} + S_{i+1,j,k} \begin{Bmatrix} u_{i+\frac{3}{2},j,k}, & \text{if } \hat{\phi}_{i+1,j,k} \notin [0,1] \\ u_{i+\frac{3}{2},j,k} + (u_{i+\frac{1}{2},j,k} - u_{i+\frac{3}{2},j,k})\hat{\phi}_{i+1,j,k}, & \text{if } \hat{\phi}_{i+1,j,k} \in [0,1] \end{Bmatrix}$$

$$\hat{\phi}_{i,j,k} = (1 - S_{i,j,k}) \left(\frac{\left(u_{i-\frac{1}{2},j,k} - u_{i-\frac{3}{2},j,k} \right)}{\left(u_{i+\frac{1}{2},j,k} - u_{i-\frac{3}{2},j,k} \right)} \right) + S_{i,j,k} \left(\frac{\left(u_{i+\frac{1}{2},j,k} - u_{i+\frac{3}{2},j,k} \right)}{\left(u_{i-\frac{1}{2},j,k} - u_{i+\frac{3}{2},j,k} \right)} \right)$$

$$u_{i,j,k} = (1 - S_{i,j,k}) \begin{Bmatrix} u_{i-\frac{1}{2},j,k}, & \text{if } \hat{\phi}_{i,j,k} \notin [0,1] \\ u_{i-\frac{1}{2},j,k} + (u_{i+\frac{1}{2},j,k} - u_{i-\frac{1}{2},j,k})\hat{\phi}_{i,j,k}, & \text{if } \hat{\phi}_{i,j,k} \in [0,1] \end{Bmatrix} + S_{i,j,k} \begin{Bmatrix} u_{i+\frac{1}{2},j,k}, & \text{if } \hat{\phi}_{i,j,k} \notin [0,1] \\ u_{i+\frac{1}{2},j,k} + (u_{i-\frac{1}{2},j,k} - u_{i+\frac{1}{2},j,k})\hat{\phi}_{i,j,k} & \text{if } \hat{\phi}_{i,j,k} \in [0,1] \end{Bmatrix}$$

SMART:

$$\hat{\phi}_{i+1,j,k} = (1 - S_{i+1,j,k}) \left(\frac{\left(u_{i+\frac{1}{2},j,k} - u_{i-\frac{1}{2},j,k} \right)}{\left(u_{i+\frac{3}{2},j,k} - u_{i-\frac{1}{2},j,k} \right)} \right) + S_{i+1,j,k} \left(\frac{\left(u_{i+\frac{3}{2},j,k} - u_{i+\frac{5}{2},j,k} \right)}{\left(u_{i+\frac{1}{2},j,k} - u_{i+\frac{5}{2},j,k} \right)} \right)$$

$$u_{i+1,j,k} = (1 - S_{i+1,j,k}) \begin{Bmatrix} u_{i+\frac{1}{2},j,k}, & \text{if } \hat{\phi}_{i+1,j,k} \notin [0,1] \\ 10u_{i+\frac{1}{2},j,k} - 9u_{i-\frac{1}{2},j,k}, & \text{if } \hat{\phi}_{i+1,j,k} \in [0,3/74) \\ \frac{3}{8}u_{i+\frac{3}{2},j,k} + \frac{6}{8}u_{i+\frac{1}{2},j,k} - \frac{1}{8}u_{i-\frac{1}{2},j,k}, & \text{if } \hat{\phi}_{i+1,j,k} \in [3/74, 5/6) \\ u_{i+\frac{3}{2},j,k}, & \text{if } \hat{\phi}_{i+1,j,k} \in [5/6, 1] \end{Bmatrix}$$

$$+S_{i+1,j,k}\begin{cases} u_{i+\frac{3}{2},j,k}, & \text{if } \hat{\phi}_{i+1,j,k}\notin[0,1] \\ 10u_{i+\frac{3}{2},j,k}-9u_{i+\frac{5}{2},j,k}, & \text{if } \hat{\phi}_{i+1,j,k}\in[0,3/74) \\ \dfrac{3}{8}u_{i+\frac{1}{2},j,k}+\dfrac{6}{8}u_{i+\frac{3}{2},j,k}-\dfrac{1}{8}u_{i+\frac{5}{2},j,k}, & \text{if } \hat{\phi}_{i+1,j,k}\in[3/74,5/6) \\ u_{i+\frac{1}{2},j,k}, & \text{if } \hat{\phi}_{i+1,j,k}\in[5/6,1] \end{cases}$$

$$\hat{\phi}_{i,j,k}=(1-S_{i,j,k})\left(\frac{\left(u_{i-\frac{1}{2},j,k}-u_{i-\frac{3}{2},j,k}\right)}{\left(u_{i+\frac{1}{2},j,k}-u_{i-\frac{3}{2},j,k}\right)}\right)+S_{i,j,k}\left(\frac{\left(u_{i+\frac{1}{2},j,k}-u_{i+\frac{3}{2},j,k}\right)}{\left(u_{i-\frac{1}{2},j,k}-u_{i+\frac{3}{2},j,k}\right)}\right)$$

$$u_{i,j,k}=(1-S_{i,j,k})\begin{cases} u_{i-\frac{1}{2},j,k}, & \text{if } \hat{\phi}_{i,j,k}\notin[0,1] \\ 10u_{i-\frac{1}{2},j,k}-9u_{i-\frac{3}{2},j,k}, & \text{if } \hat{\phi}_{i,j,k}\in[0,3/74) \\ \dfrac{3}{8}u_{i+\frac{1}{2},j,k}+\dfrac{6}{8}u_{i-\frac{1}{2},j,k}-\dfrac{1}{8}u_{i-\frac{3}{2},j,k}, & \text{if } \hat{\phi}_{i,j,k}\in[3/74,5/6) \\ u_{i+\frac{1}{2},j,k}, & \text{if } \hat{\phi}_{i,j,k}\in[5/6,1] \end{cases}$$

$$+S_{i,j,k}\begin{cases} u_{i+\frac{1}{2},j,k}, & \text{if } \hat{\phi}_{i,j,k}\notin[0,1] \\ 10u_{i+\frac{1}{2},j,k}-9u_{i+\frac{3}{2},j,k}, & \text{if } \hat{\phi}_{i,j,k}\in[0,3/74) \\ \dfrac{3}{8}u_{i-\frac{1}{2},j,k}+\dfrac{6}{8}u_{i+\frac{1}{2},j,k}-\dfrac{1}{8}u_{i+\frac{3}{2},j,k}, & \text{if } \hat{\phi}_{i,j,k}\in[3/74,5/6) \\ u_{i-\frac{1}{2},j,k}, & \text{if } \hat{\phi}_{i,j,k}\in[5/6,1] \end{cases}$$

VONOS:

$$\hat{\phi}_{i+1,j,k}=(1-S_{i+1,j,k})\left(\frac{\left(u_{i+\frac{1}{2},j,k}-u_{i-\frac{1}{2},j,k}\right)}{\left(u_{i+\frac{3}{2},j,k}-u_{i-\frac{1}{2},j,k}\right)}\right)+S_{i+1,j,k}\left(\frac{\left(u_{i+\frac{3}{2},j,k}-u_{i+\frac{5}{2},j,k}\right)}{\left(u_{i+\frac{1}{2},j,k}-u_{i+\frac{5}{2},j,k}\right)}\right)$$

$$u_{i+1,j,k}=(1-S_{i+1,j,k})\begin{cases} u_{i+\frac{1}{2},j,k}, & \text{if } \hat{\phi}_{i+1,j,k}\notin[0,1] \\ 10u_{i+\frac{1}{2},j,k}-9u_{i-\frac{1}{2},j,k}, & \text{if } \hat{\phi}_{i+1,j,k}\in[0,3/74) \\ \dfrac{3}{8}u_{i+\frac{3}{2},j,k}+\dfrac{6}{8}u_{i+\frac{1}{2},j,k}-\dfrac{1}{8}u_{i-\frac{1}{2},j,k}, & \text{if } \hat{\phi}_{i+1,j,k}\in[3/74,1/2) \\ 1.5u_{i+\frac{1}{2},j,k}-0.5u_{i-\frac{1}{2},j,k}, & \text{if } \hat{\phi}_{i+1,j,k}\in[1/2,2/3) \\ u_{i+\frac{3}{2},j,k}, & \text{if } \hat{\phi}_{i+1,j,k}\in[2/3,1] \end{cases}$$

$$+S_{i+1,j,k}\begin{cases} u_{i+\frac{3}{2},j,k}, & \text{if } \hat{\phi}_{i+1,j,k}\notin[0,1] \\ 10u_{i+\frac{3}{2},j,k}-9u_{i+\frac{3}{2},j,k}, & \text{if } \hat{\phi}_{i+1,j,k}\in[0,3/74) \\ \dfrac{3}{8}u_{i+\frac{1}{2},j,k}+\dfrac{6}{8}u_{i+\frac{3}{8},j,k}-\dfrac{1}{8}u_{i+\frac{5}{2},j,k}, & \text{if } \hat{\phi}_{i+1,j,k}\in[3/74,1/2) \\ 1.5u_{i+\frac{3}{2},j,k}-0.5u_{i+\frac{5}{2},j,k}, & \text{if } \hat{\phi}_{i+1,j,k}\in[1/2,2/3) \\ u_{i+\frac{1}{2},j,k}, & \text{if } \hat{\phi}_{i+1,j,k}\in[2/3,1] \end{cases}$$

$$\hat{\phi}_{i,j,k} = (1 - S_{i,j,k}) \left(\frac{\left(u_{i-\frac{1}{2},j,k} - u_{i-\frac{3}{2},j,k} \right)}{\left(u_{i+\frac{1}{2},j,k} - u_{i-\frac{3}{2},j,k} \right)} \right) + S_{i,j,k} \left(\frac{\left(u_{i+\frac{1}{2},j,k} - u_{i+\frac{3}{2},j,k} \right)}{\left(u_{i-\frac{1}{2},j,k} - u_{i+\frac{3}{2},j,k} \right)} \right)$$

$$u_{i,j,k} = (1 - S_{i,j,k}) \begin{cases} u_{i-\frac{1}{2},j,k}, & \text{if } \hat{\phi}_{i,j,k} \notin [0,1] \\ 10u_{i-\frac{1}{2},j,k} - 9u_{i-\frac{3}{2},j,k}, & \text{if } \hat{\phi}_{i,j,k} \in [0,3/74) \\ \frac{3}{8}u_{i+\frac{1}{2},j,k} + \frac{6}{8}u_{i-\frac{1}{2},j,k} - \frac{1}{8}u_{i-\frac{3}{2},j,k}, & \text{if } \hat{\phi}_{i,j,k} \in [3/74,1/2) \\ 1.5u_{i-\frac{1}{2},j,k} - 0.5u_{i-\frac{3}{2},j,k}, & \text{if } \hat{\phi}_{i,j,k} \in [1/2,2/3) \\ u_{i+\frac{1}{2},j,k}, & \text{if } \hat{\phi}_{i,j,k} \in [2/3,1] \end{cases}$$

$$+ S_{i,j,k} \begin{cases} u_{i+\frac{1}{2},j,k}, & \text{if } \hat{\phi}_{i,j,k} \notin [0,1] \\ 10u_{i+\frac{1}{2},j,k} - 9u_{i+\frac{3}{2},j,k}, & \text{if } \hat{\phi}_{i,j,k} \in [0,3/74) \\ \frac{3}{8}u_{i-\frac{1}{2},j,k} + \frac{6}{8}u_{i+\frac{1}{2},j,k} - \frac{1}{8}u_{i+\frac{3}{2},j,k}, & \text{if } \hat{\phi}_{i,j,k} \in [3/74,1/2) \\ 1.5u_{i+\frac{1}{2},j,k} - 0.5u_{i+\frac{3}{2},j,k}, & \text{if } \hat{\phi}_{i+1,j,k} \in [1/2,2/3) \\ u_{i-\frac{1}{2},j,k}, & \text{if } \hat{\phi}_{i,j,k} \in [2/3,1] \end{cases}$$

7. NUMERICAL RESULTS FOR 3D NAVIER–STOKES EQUATION

In Section 5 we provided numerical calculations using the axiysmmetric code. The essential two-dimensional nature of this code permitted good resolution, so much so that we were able to demonstrate the single and double roller effects in the circular-hydraulic jump. Unfortunately, although this quality of resolution is not yet possible for a time-dependent three-space dimensional code, Freeflow3D has the advantage of a customized solid modelling visualization facility. This provides immediate and dramatic feedback on the various convective approximants, as it can be seen from Figures 11–15. The various convection schemes presented

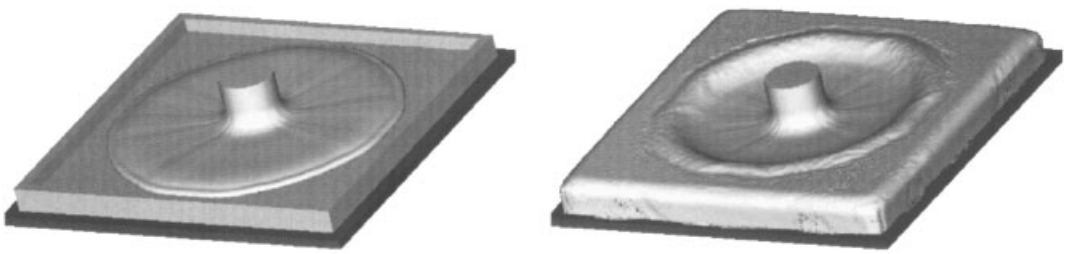

Figure 11. 3D simulation using the VONOS scheme showing: (a) the geometry and the free-surface at time $t = 0.138$ s; (b) free-surface at time $t = 0.588$ s.

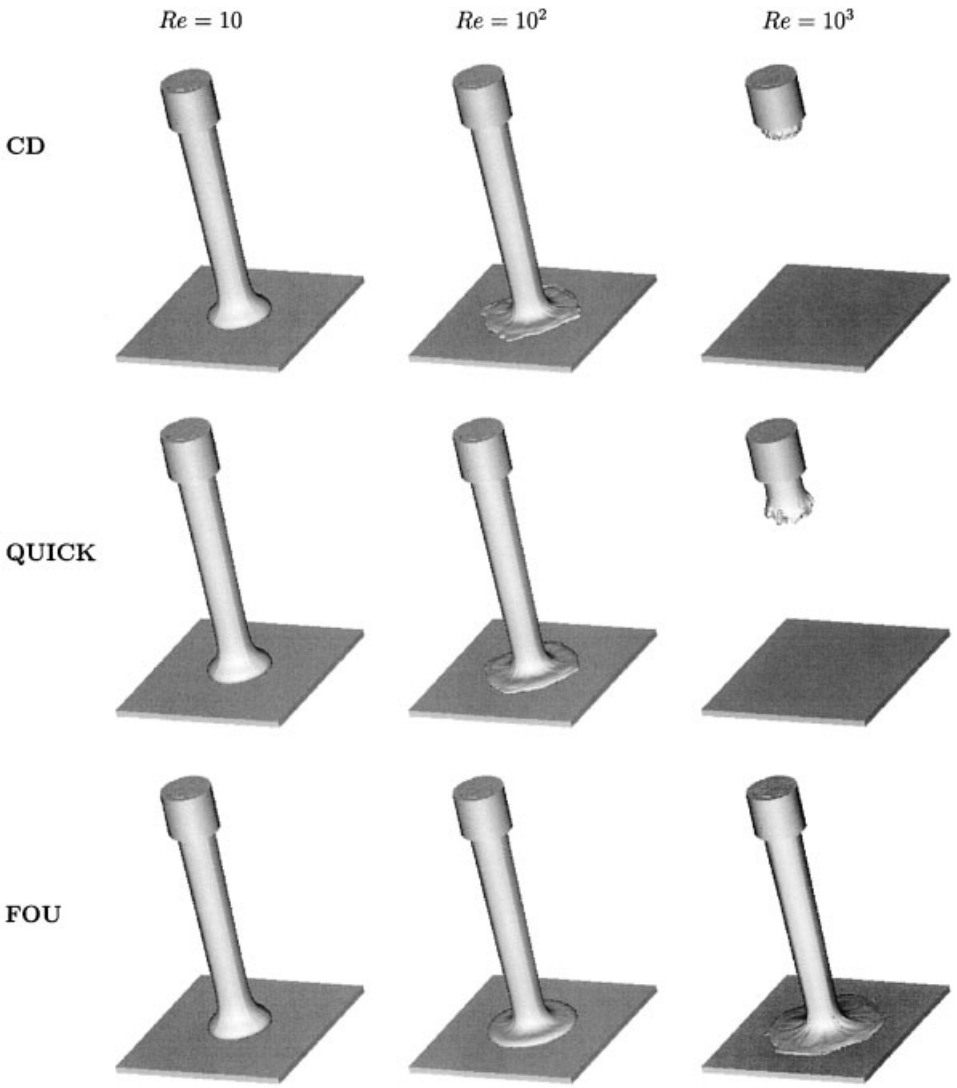

Figure 12. Three-dimensional view of the numerical simulation of an axisymmetric jet impinging onto a horizontal flat surface at $t = 0.035$ s for increasing Reynolds numbers and using the various convection schemes. First column: $Re = 10$; second column: $Re = 10^2$; third column: $Re = 10^3$.

in Section 3 have been implemented in the Freeflow3D code and the code has been used to simulate the flow of a jet impinging onto a flat surface at increasing Reynolds numbers. Two shapes of jets were considered: an axisymmetric and a planar jet. In addition, in order to study the relative effectiveness of these convective approximations, we applied the code to simulate the phenomenon of the circular-hydraulic jump with a Newtonian fluid at $Re = 400$. The results are as follows.

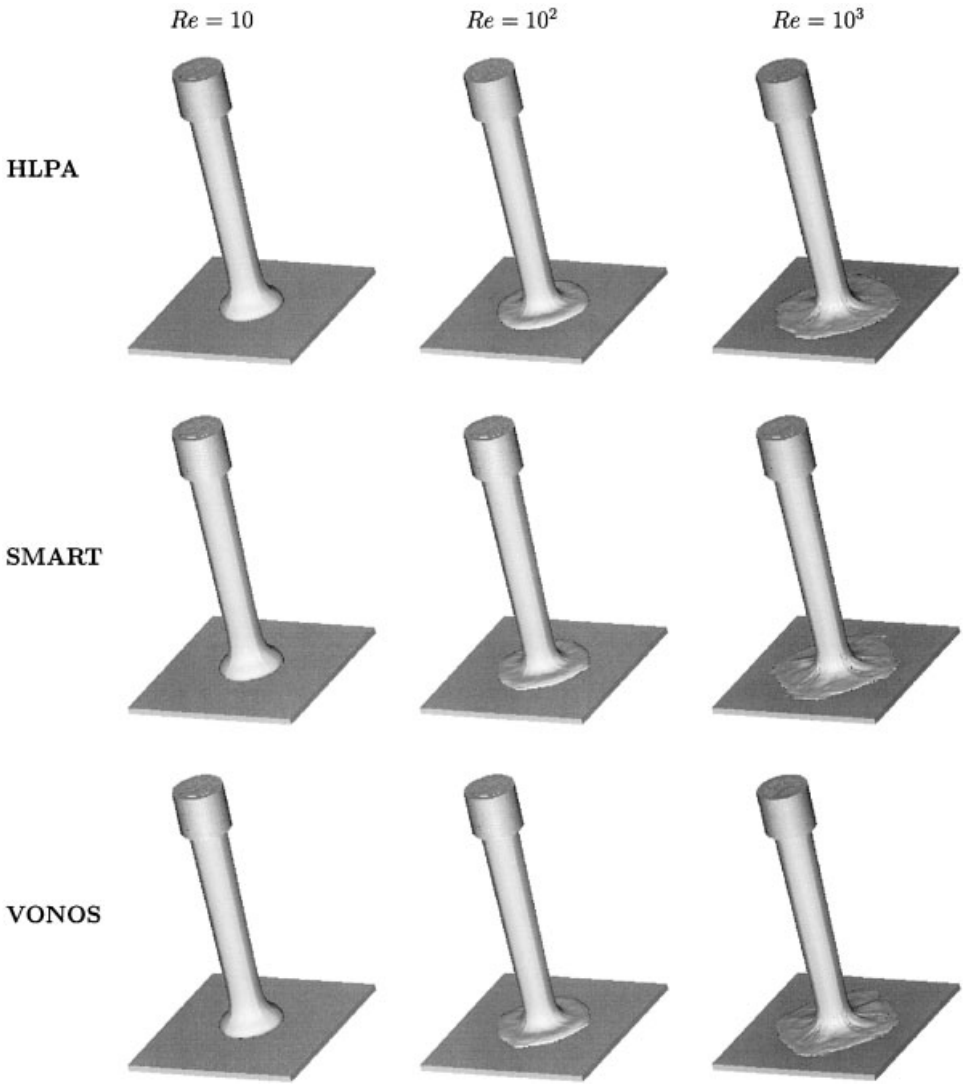

Figure 12. (*Continued*)

7.1. Simulation of the axisymmetric jet onto a flat plate

An axisymmetric jet of viscous fluid was projected onto a horizontal surface at a prescribed velocity. The following input data were used:

- Domain dimensions: $0.04\,\text{m} \times 0.04\,\text{m} \times 0.06\,\text{m}$;
- Mesh size: $80 \times 80 \times 120$ cells ($\delta x = \delta y = \delta z = 0.0005\,\text{m}$);
- Flat surface dimensions: $0.04\,\text{m} \times 0.04\,\text{m} \times 0.0015\,\text{m}$;
- Inflow dimensions: diameter $(\text{D}) = 0.008\,\text{m}$ and height $(\text{h}) = 0.01\,\text{m}$; The inflow is situated at a distance of $0.05\,\text{m}$ above the flat surface;

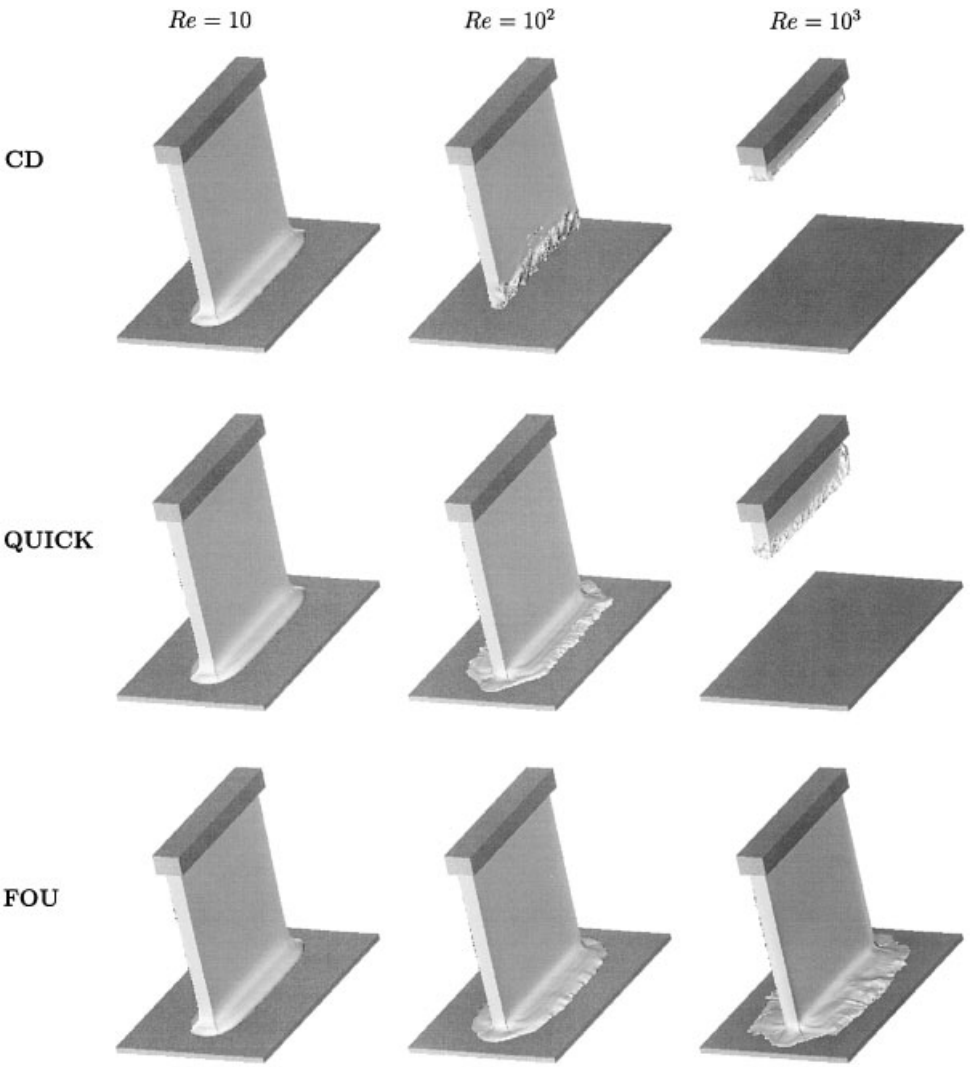

Figure 13. Three-dimensional view of the numerical simulation of a planar jet impinging onto a horizontal flat surface at $t = 0.045$ s for increasing Reynolds numbers and using the various convection schemes. First column: $Re = 10$; second column: $Re = 10^2$; third column: $Re = 10^3$.

- Inflow velocity: $U_0 = 1\ \mathrm{ms}^{-1}$;
- Scaling parameters: $U_0 = 1\ \mathrm{ms}^{-1}$, $\mathrm{D} = 0.008$ m;
- Gravity was acting in the z-direction, with $g = -9.81\ \mathrm{ms}^{-2}$;
- Froude number: $Fr = 3.569$;
- Convergence criterion for the conjugate gradient methods: $\mathrm{EPS} = 10^{-7}$.

The Freeflow3D code simulated the problem described above using each of the schemes: FOU, CD, QUICK, SMART, HLPA and VONOS. The following values of the kinematic

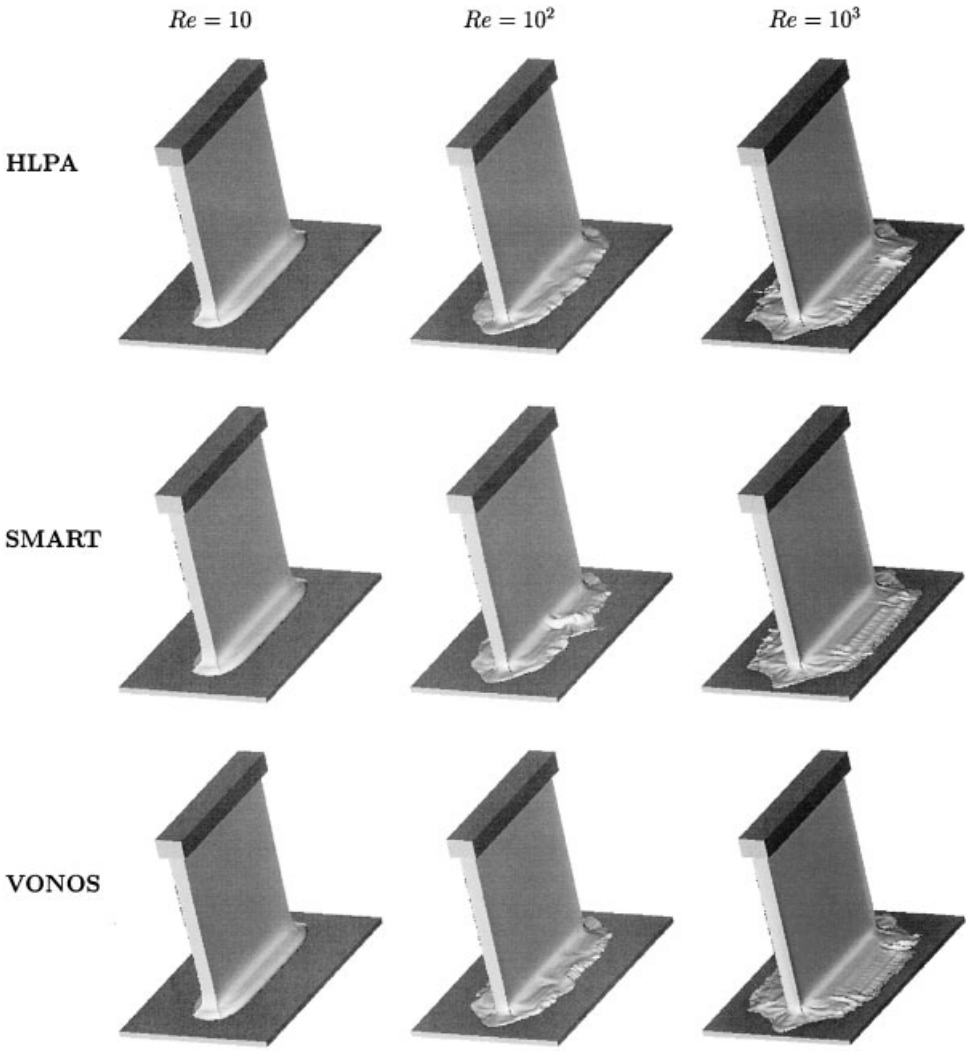

Figure 13. (*Continued*)

viscosity $v = 8 \times 10^{-4}$, 8×10^{-5} and $8 \times 10^{-6}\,\mathrm{m^2\,s^{-1}}$ were used. These produced Reynolds numbers of 10, 10^2 and 10^3, respectively. A time-step size of $\delta t \approx 10^{-6}\,\mathrm{s}$ was used in all these runs (it is, of course, not possible to be precise here, since the code employs an automatic time-step generator (see Tomé and McKee [4])). In total, 18 runs were performed, six for each Reynolds number. It should be stressed that, except for the Reynolds number and the type of upwinding, all runs were identical. The results of these runs are summarized in Figure 12. This figure displays the fluid flow visualization at $t = 0.035\,\mathrm{s}$ using each of the schemes above for each Reynolds number. Row CD shows the results obtained by the CD approach and row FOU displays the results of the FOU scheme. In the same way, rows QUICK, SMART, VONOS and HLPA show the corresponding results of the QUICK, SMART, VONOS and

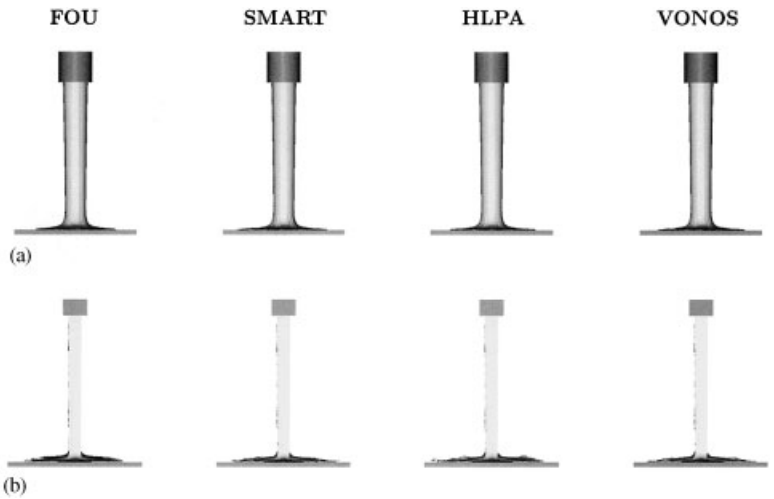

Figure 14. Front view of the numerical simulations of two jets impinging onto a horizontal flat surface ($Re = 10^3$): (a) axisymmetric jet at $t = 0.035$ s; (b) planar jet at $t = 0.045$ s.

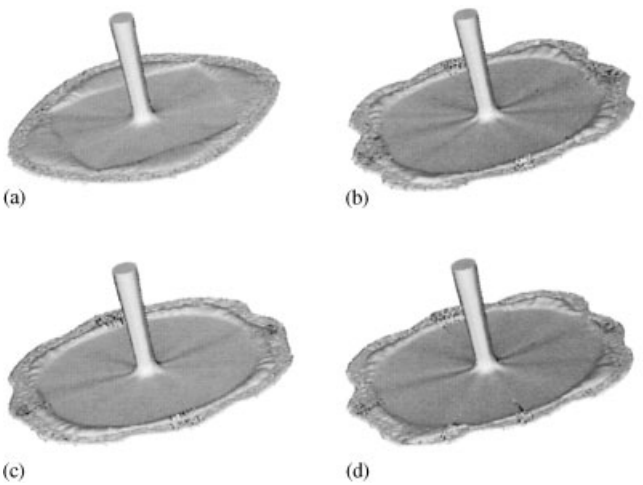

Figure 15. 3D view of the numerical simulation of a circular-hydraulic jump at $t = 0.30$ s, $Re = 4 \times 10^2$ and $Fr = 1.785$: (a) FOU; (b) SMART; (c) HLPA and (d) VONOS.

HLPA methods, respectively. Due to instability, some schemes (e.g. CD and QUICK) did not reach the final time ($t = 0.035$ s), when the Reynolds number became sufficiently large.

7.2. Simulation of the planar jet

A planar jet of viscous fluid was projected onto a horizontal surface with a prescribed velocity. The following input data were employed:

- Domain dimensions: $0.04\,\text{m} \times 0.06\,\text{m} \times 0.05\,\text{m}$;
- Mesh size: $80 \times 120 \times 100$ cells ($\delta x = \delta y = \delta z = 0.0005\,\text{m}$);
- Flat surface dimensions: $0.04\,\text{m} \times 0.06\,\text{m} \times 0.0015\,\text{m}$;
- Inflow dimensions: $0.004\,\text{m} \times 0.04\,\text{m}$ and height (h) $= 0.005\,\text{m}$. The inflow is situated at a distance of 0.45 m above the flat surface;
- Inflow velocity: $U_0 = 1\,\text{ms}^{-1}$;
- Scaling parameters: $U_0 = 1\,\text{ms}^{-1}$; D $= 0.004\,\text{m}$;
- Gravity was acting in the z-direction, with $g = -9.81\,\text{ms}^{-2}$;
- Froude number: $Fr = 5.048$;
- Convergence criterion for the conjugate gradient method: EPS $= 10^{-8}$.

The code was run on this problem with the above input data. The values of the coefficient of viscosity were $v = 4 \times 10^{-4}$, 4×10^{-5} and $4 \times 10^{-6}\,\text{m}^2\,\text{s}^{-1}$, which resulted in Reynolds numbers of $Re = 10$, 10^2 and 10^3, respectively. A time-step size of $\delta t \approx 10^{-6}$ s was used in all these runs. Figure 13 displays the results of the various schemes at time $t = 0.045$ s.

7.3. Simulation of the circular-hydraulic jump

An axisymmetric jet of viscous fluid was projected onto a horizontal surface with an appropriate prescribed velocity, so that a hydraulic jump would occur. The following input data were used in this simulation:

- Domain dimensions: $0.1\,\text{m} \times 0.1\,\text{m} \times 0.1\,\text{m}$;
- Mesh size: $100 \times 100 \times 100$ cells ($\delta x = \delta y = \delta z = 0.001\,\text{m}$);
- Solid surface dimensions: $0.1\,\text{m} \times 0.1\,\text{m} \times 0.0015\,\text{m}$;
- Inflow dimensions: diameter (D) $= 0.008\,\text{m}$ and height (h) $= 0.02\,\text{m}$. The inflow is situated at a distance of 0.048 m above of the solid surface;
- Inflow velocity: $U_0 = 0.05\,\text{ms}^{-1}$;
- Scaling parameters: $U_0 = 0.05\,\text{ms}^{-1}$, D $= 0.008\,\text{m}$;
- Gravity was acting in the z-direction, with $g = -9.81\,\text{ms}^{-2}$;
- Kinematic viscosity: $v = 10^{-5}\,\text{m}^2\,\text{s}^{-1}$;
- Froude number: $Fr = 1.785$;
- Reynolds number: $Re = 400$;
- Convergence criterion for the conjugate gradient method: EPS $= 10^{-8}$.

The Freeflow3D code was run on this problem with the above input data for the various convection schemes presented in Section 3. We point out that the CD and the QUICK schemes failed as the jet was destroyed due to numerical instabilities. The other schemes; namely, FOU, SMART, HLPA and VONOS, did not display any instability and the phenomenon of the hydraulic jump was successfully simulated. Figure 15 exhibits a three-dimensional view of the results of these runs at time $t = 0.30$ s.

As we can see from Figures 12 and 13 for low-Reynolds number ($Re = 10$), the six schemes produced similar results, with no sign of numerical instability. However, as the Reynolds number was increased, both CD and QUICK caused the methods to fail to converge due to numerical instabilities. Indeed, from these figures, it can be observed that the CD method failed for the axisymmetric jet at $Re = 10^3$, and also failed for the simulation of the planar jet at $Re = 10^2$ and $Re = 10^3$. The QUICK scheme, although a third-order method, could not cope with a high-Reynolds number jet. This might have been expected of these schemes, since

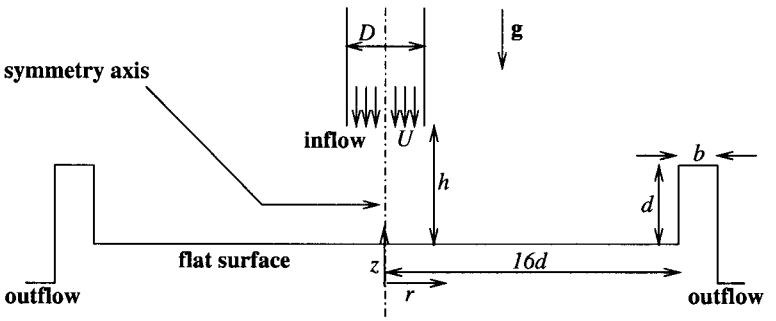

Figure 16. Axisymmetric geometry showing parameters and dimensions: $D = 0.02$ m; $U_0 = 0.75\ \mathrm{m\ s^{-1}}$, $h = 0.01$; $d = 0.005$; $b = 0.00375$.

they do not unconditionally satisfy the CBC. On the other hand, FOU, SMART, VONOS and HLPA produced oscillation-free results at high-Reynolds numbers (e.g. $Re = 10^3$). Nevertheless, as one can infer from the pictures the FOU scheme introduces significant artificial viscosity; this is more visible for the case of $Re = 10^3$, where one can observe that the jet does not spread out as much as the SMART, VONOS or HLPA schemes. This is more noticeable when we look at the front view for both axisymmetric and planar jets, as shown in Figure 14.

In the simulation of the complex flow of a circular-hydraulic jump, the CD and QUICK schemes did not succeed. The other schemes FOU, SMART, VONOS and HLPA coped well with this problem and did not display any numerical instabilities. However, as we can see in Figure 15, the FOU scheme did not produce a circular radius due, we believe, to excessive numerical dissipation. SMART, VONOS and HLPA presented a good simulation of the circular-hydraulic jump. This confirms the usefulness of these upwind schemes for simulating complicated free-surface flows since they are at least second-order accurate, satisfy the CBC and introduce less numerical viscosity than FOU.

7.4. Comparison between the axisymmetric and 3D numerical simulations

We conclude this paper by comparing a full 3D numerical simulation with the axisymmetric one. In both the axisymmetric and the 3D codes, the FOU and VONOS schemes were used for the simulation of the circular-hydraulic jump with the geometry and parameters shown in Figure 16. In order to compare the 3D and the axisymmetric solutions with Watson's solution, the position $r = r_1$ of the jump, given by Equations (5) and (6), was computed. The parameters of the simulations were $Re = 150$ and $Fr = 1.693$. The mesh sizes used were 55×22 cells ($\delta r = \delta z = 0.00125$ m) in the axisymmetric case and $110 \times 110 \times 22$ cells ($\delta x = \delta y = \delta z = 0.00125$ m) in the 3D problem. Figure 11(a) shows the geometry of the equivalent 3D problem and the fluid flowing on the open-box container at time $t = 0.138$ s. From this figure we see that both the rigid-boundary on which the fluid is impinging and the outflow-boundary through which the fluid is leaving are square. Figure 11(b) shows the free-surface of the flow computed with the VONOS scheme at final time $t = 0.588$ s. Next, several different cross-sections from the 3D simulation are compared with the axisymmetric calculations.

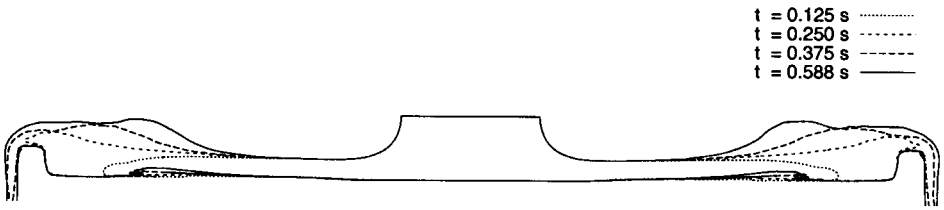

Figure 17. 3D-transient free-surface profile along the $x-z$ plane at position $y = 0.0$.

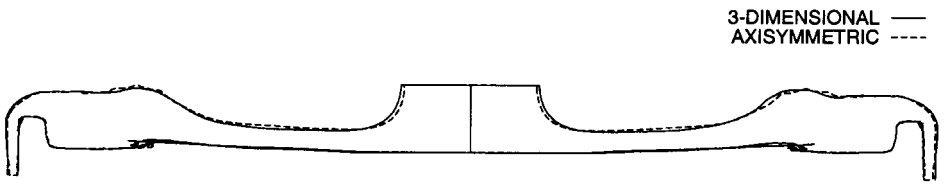

Figure 18. Comparison, at time $t = 0.588$ s, between the 3D free-surface profile along the x–z plane at position $y = 0.0$ and axisymmetric profile.

Figure 17 shows the time-dependent free-surface profile, along the x–z plane at position $y = 0.0$, for the 3D simulation using the VONOS scheme. It can be inferred, from this figure, that the location of the jump approaches the steady-state value given by the axisymmetric simulation. We have not been able to reach the 3D steady-state solution due to machine-memory limitations; at the last time level ($t = 0.588$ s) the memory requirements exceeded 1.3 GB.

Figure 18 displays a comparison between the 3D free-surface profile, along the x–z plane at position $y = 0.0$, and the axisymmetric results, both using the VONOS scheme. The agreement between the two profiles is good, even though the 3D-container has been chosen to be a square and not a cylindrical-open box.

We compare several different cross-sections from the 3D results with the axisymmetric results to bring out grid orientation effects. Figure 19 displays cross-sections of the 3D simulation with the VONOS scheme at planes 30, 45 and 90 degrees with respect to the x–z plane. These cross-sections show that the distance of the jump location to the stagnation points is the same for the three cross-sections. Furthermore, there is a good agreement between these free-surface profiles and that shown in Figure 18 with 0 degree rotation. The small differences in the length of the flow downstream of the jump, appearing in the 30° and 45° profiles, would appear to be by the fact that the container cross-section in the 3D simulation is not circular, but square.

Finally, Figures 20 and 21 show respectively cross-sections, parallel to the x–y plane at the vertical location $z = 0.01247$, of the 3D numerical solution using the VONOS and FOU schemes. This location corresponds to the average between the location of the free-surface before and after the jump, i.e., the location of the middle point of the jump. For comparison, both cross-sections are overlayed with the equivalent axisymmetric solution of the same problem, and the approximate analytical location of the jump ($r_1 = 0.03308$). Once more the agreement between the two numerical solutions by using the VONOS scheme is really quite

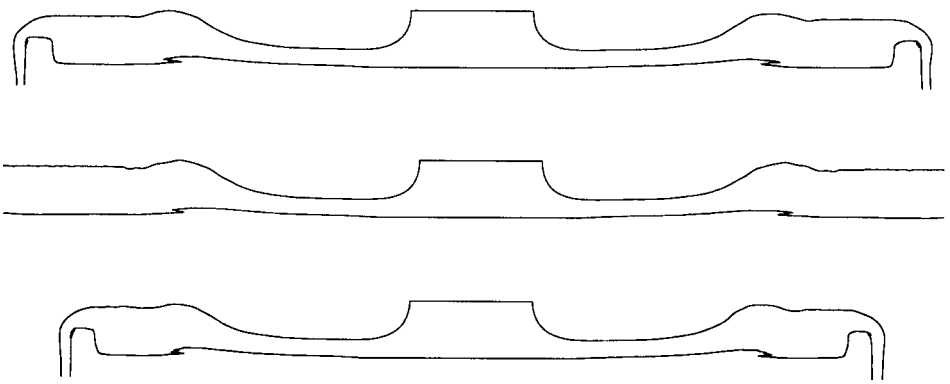

Figure 19. Cross-sections of the 3D free-surface simulation. The top, middle, and bottom profiles correspond to the 30, 45 and 90 degree rotations, respectively.

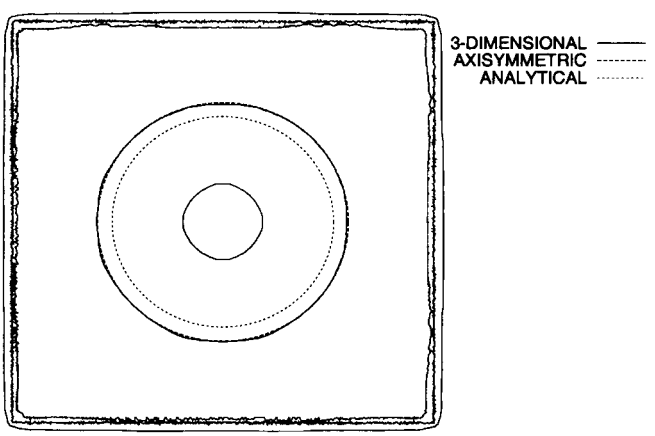

Figure 20. Parallel cross-sections to the x–y plane, at position $z = 0.01247$, of the 3D and axisymmetric numerical solutions, and approximate analytical value of the jump position. The VONOS scheme was used to discretize the convective terms.

good. It can also be observed that the VONOS scheme produces an almost perfectly circular hydraulic jump, indicating that grid orientation effects are small. On the other hand, the FOU scheme is particularly poor in this regard.

8. DISCUSSION OF THE RESULTS AND CONCLUSIONS

In this paper we have introduced the axisymmetric GENSMAC and the Freeflow3D codes, two closely related computer programs based on the marker and cell ideas. These codes have been adapted to employ different high-order upwind discretizations. One of the main purposes of this paper was to effect a comparison between the many existing convective approximations on a real problem.

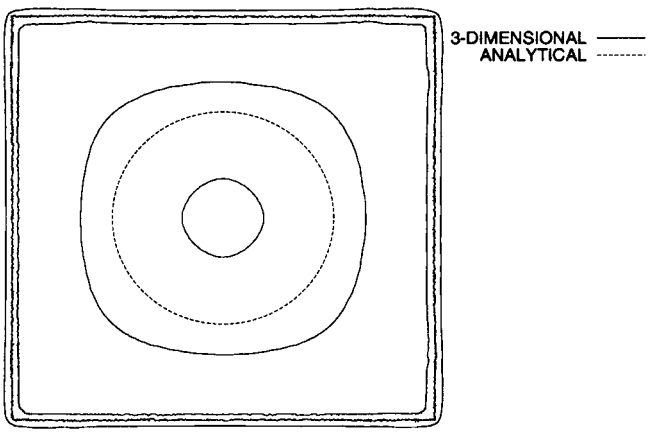

Figure 21. Parallel cross-sections to the x–y plane, at position $z = 0.01247$, of the 3D and approximate analytical value of the jump position. The FOU scheme was used to discretize the convective terms.

The real problem chosen was the circular-hydraulic jump. The single and double roller in the jump were simulated by the axisymmetric GENSMAC and displayed qualitative agreement with the experimental observations. A comparison was also made with the approximate analytical solutions given by Watson and a quantitative agreement was obtained.

We are conscious that the numerical experiments described in this paper are not enough to fully validate Freeflow3D. This is at present difficult as mesh refinement soon becomes intractable. However, we would argue that there has been a degree of qualitative validation. Figure 11(b) displays the hydraulic jump in the same radial position as that given by the axisymmetric code. There is also qualitative agreement with Watson's results, although one would be wise to regard this with some caution. Previous work [2] on the 3D code displayed three-dimensional jet buckling with coiling as well as planar folding which are at least credible and what we expect from our earlier experimental work [38].

The best, and possibly the only acceptable, upwind methods emerging from this study are SMART, VONOS and HLPA. These composite differencing schemes for the convection terms are a good compromise between numerical stability and accuracy. On the other hand, both CD and QUICK broke down, while the FOU always worked but it always introduced too much artificial viscosity.

It is perhaps worth emphasizing that the circular-hydraulic jump obtained from Freeflow3D uses x, y and z coordinates and has no in-built assumption of axisymmetry. Thus, in principle, it should be capable of capturing polygonal-hydraulic jumps that were observed by Craik *et al.* [15] and, more recently, by Ellegaard *et al.* [20, 21].

A hydraulic jump is a relatively abrupt phenomenon described by a nonlinear interaction between the effects of viscosity and the inviscid mechanisms of surface tension, cross-stream pressure gradients induced by streamline curvature, and gravity. Both the codes discussed here do not as yet have surface tension implemented. However, this work is underway and we believe we are not far away from capturing, and possibly completely characterizing the hydraulic jump at least for moderate Reynolds numbers.

ACKNOWLEDGEMENTS

We gratefully acknowledge the support given by FAPESP (Fundação de Amparo à Pesquisa do Estado de São Paulo) and CNPq (Conselho Nacional de Desenvolvimento Científico e Tecnológico). The last author (SMcK) would like to acknowledge support from the Royal Society of Edinburgh.

REFERENCES

1. Tomé MF, Castelo AF, Murakami J, Cuminato JA, Minghim R, Oliveira CF, Mangiavacchi N, McKee S. Numerical simulation of axisymmetric free surface flows. *Journal of Computational Physics* 2000; **157**: 441–472.
2. Castelo AF, Tomé MF, César CNL, McKee S, Cuminato JA. Freeflow: an integrated simulation system for three-dimensional free surface flows. *Computing and Visualization in Science* 1999; **2**:1–12.
3. Tomé MF, Castelo AF, Cuminato JA, McKee S. GENSMAC3D: A numerical method for solving three-dimensional free surface flows. *International Journal for Numerical Methods in Fluids* 2001; **37**:747–796.
4. Tomé MF, McKee S. GENSMAC: A computational marker-and-cell method for free surface flows in general domains. *Journal of Computational Physics* 1994; **110**:171–186.
5. Welch JE, Harlow FH, Shannon JP, Daly BJ. The MAC method. *Los Alamos Scientific Laboratory Report LA-3425*, 1965.
6. Amsden A, Harlow F. The SMAC method: a numerical technique for calculating incompressible fluid flows. *Los Alamos Scientific Laboratory Report LA-4370*, 1970.
7. Watson EJ. The radial spread of a liquid jet over a horizontal plane. *Journal of Fluid Mechanics* 1964; **20**: 481–499.
8. Yokoi K, Xiao F. A numerical study of the transition in the circular hydraulic jump. *Physics Letters A* 1999; **257**:153–157.
9. Zhou JG, Stansby PK. 2D shallow water flow model for the hydraulic jump. *International Journal for Numerical Methods in Fluids* 1999; **29**:375–387.
10. Lord Rayleigh. On the theory of long waves and bores. *Proceedings of the Royal Society of London, Series A* 1914; **90**:324–328.
11. Kurihara M. A consideration about hydraulic jump. *Report of the Research Institution on Fluids and Engineering, Kyusyu Imperial University* 1946; **3**:11.
12. Tani I. Flow separation in thin liquid layers. *Journal of the Physics Society of Japan* 1948; **4**:212–215.
13. Olsson RG, Turkdogan ET. Radial spread of a liquid stream on a horizontal plate. *Nature* 1966; **211**:813–816.
14. Ishigai S, Nakanishi S, Mizuno M, Imamura T. Heat transfer of the impinging round water jet in the interference zone of film flow along the wall. *Bulletin of the JSME* 1977; **20**:85–92.
15. Craik AD, Latham RC, Fawkes MJ, Gribbon WF. The circular hydraulic jump. *Journal of Fluid Mechanics* 1981; **112**:347–362.
16. Errico M. A study of the interaction of liquid jets with solid surfaces. *Ph.D. Thesis*, University of California at San Diego, 1986.
17. Vasista VK. Experimental study of the hydrodynamics of an impinging liquid jet. *S.B. Thesis*, Massachusetts Institute of Technology, 1989.
18. Thomas S, Faghri A, Hankey W. Experimental analysis and flow visualization of a thin liquid film on a stationary and rotating disk. *Transactions of the ASME Journal on Fluids Engineering* 1999; **113**:73–80.
19. Bohr T, Putkaradze V, Watanabe W. Averaging theory for the structure of hydraulic jumps and separation in laminar free surface flows. *Physics Review Letters* 1997; **79**:1038–1041.
20. Ellegaard C, Hansen AE, Haaning A, Hansen K, Marcussen A, Bohr T, Hansen JL, Watanabe S. Creating corners in kitchen sinks. *Nature* 1998; **392**:767–768.
21. Ellegaard C, Hansen AE, Haaning A, Hansen K, Marcussen A, Bohr T, Hansen JL, Watanabe S. Cover illustration: Polygonal hydraulic jumps. *Nonlinearity* 1999; **12**:1–7.
22. Liu X, Lienhard V. The hydraulic jump in circular jet impingement and in other thin liquid films. *Experiments in Fluids* 1993; **15**:108–116.
23. Gajjar JSB, Smith FT. On the hypersonic self-induced separation hydraulic jumps and boundary layers with algebraic growth. *Mathematika* 1983; **30**:77–86.
24. Bowles RI, Smith FT. The standing hydraulic jump: theory computations and comparisons with experiments. *Journal of Fluid Mechanics* 1992; **242**:145–168.
25. Higuera FJ. The hydraulic jump in a viscous laminar flow. *Journal of Fluid Mechanics* 1994; **274**:69–92.
26. Higuera FJ. The circular hydraulic jump. *Physics of Fluids* 1997; **9**:1476–1478.
27. Schlichting H. *Boundary Layer Theory*. McGraw-Hill: New York, 1968.
28. Price HS, Varga RS, Warren JE. Applications of oscillation matrices to diffusion–correction equations. *Journal of Mathematical Physics* 1966; **45**:301–311.

29. Khosla PK, Rubin SG. A diagonally dominant second-order accurate implicit scheme. *Computational Fluids* 1974; **2**:207–209.
30. Leonard BP. A stable and accurate convective modelling procedure based on quadratic upstream interpolation. *Computational Methods and Applications in Mechanical Engineering* 1979; **19**:59–98.
31. Gaskell PH, Lau AKC. Curvature-compensated convective transport: SMART, a new boundedness-preserving transport algorithm. *International Journal for Numerical Methods in Fluids* 1988; **8**:617–641.
32. Zhu J. On the higher-order bounded discretization schemes for finite volume computations of incompressible flows. *Computational Methods and Applications in Mechanical Engineering* 1992; **98**:345–360.
33. Varonos A, Bergeles G. Development and assessment of a variable-order non-oscillatory scheme for convection term discretization. *International Journal for Numerical Methods in Fluids* 1998; **26**:1–16.
34. Papadakis G, Bergeles G. A locally modified second order upwind scheme for convection terms discretized. *International Journal for Numerical Methods in Heat and Fluid Flow* 1995; **5**:49–62.
35. Pascau A, Perez C. A well-behaved scheme to model strong convection in a general transport equation. *Numerical Mathematics of Laminar and Turbulent Flows* 1993; **8**:608–617.
36. Batchelor GK. *An Introduction to Fluid Dynamics.* Cambridge Univ. Press: Cambridge, 1967.
37. Ortega JM. *Introduction to Parallel and Vector Solution of Linear Systems*. Plenum Press: New York, 1988.
38. Tomè MF, McKee S, Barratt L, Jarvis DA, Patrick AJ. An experimental and numerical investigation of container filling: viscous liquids. *International Journal for Numerical Methods in Fluids* 1999; **31**:1333–1353.

